

PWM-based Transthoracic Bioimpedance Analyzer for Detecting Heart Failures

Brian Nanhekhan



PWM-based Transthoracic Bioimpedance Analyzer for Detecting Heart Failures

by

Brian Hanief Tufail Nanhekhani

to obtain the degree of Master of Science
at the Delft University of Technology,
to be defended publicly on Friday August 13, 2021 at 15:30 PM.

Student number: 4175735
Project duration: November 1, 2019 – August 12, 2021
Thesis committee: Prof. dr. ir. W.A. Serdijn, TU Delft
Dr. V. Valente, Ryerson University, daily supervisor
Dr. ir. C.J.M. Verhoeven, TU Delft

This thesis is confidential and cannot be made public until September 1, 2022.

An electronic version of this thesis is available at <http://repository.tudelft.nl/>.

Abstract

Patients that suffer from heart failure can benefit from wearable monitoring devices that continuously monitor the condition of the heart. One of the foremost symptoms of exacerbation of the heart is fluid congestion in the lungs. One of the methods to measure a change in biological tissue, such as the build-up of fluids in the lungs and chest, is bioimpedance measurements. By injecting an alternating current into the tissue, a voltage develops across the tissue that is proportional to the impedance of the biological tissue, the bioimpedance. Conventional bioimpedance measurement techniques are not suitable for continuous monitoring of the patients as they are power consuming and hinder patient in their daily living.

This thesis proposes an alternative approach that is based on a pulse width modulation (PWM) in order to convert the measured analog signals to time signals. To determine the measured bioimpedance, the magnitude and phase should be derived. The proposed design employs one channel to convert the measured voltage across the bioimpedance to a PWM signal. As this PWM signal contains the amplitude information of the measured voltage, the magnitude of the bioimpedance can be derived. Furthermore, a second reference channel is employed where a known resistive reference is converted to another PWM signal. By comparing the two PWM signals, the phase of the bioimpedance can be determined. The proposed system requires only a comparator and triangular wave in order to convert the measured analog signals, compared to the complex implementation of the conventionally used analog-to-digital converter.

In order to validate the design, the circuit is simulated and implemented on a printed circuit board (PCB). The PCB operates correctly on 3.3V and, additionally, a voltage-controlled current source is implemented and connected externally to the PCB to provide an excitation current of 100 μ A and 10 kHz to the circuit. The circuit should be capable of measuring the voltage across a device under test (*DUT*) that consist of resistive and capacitive components. This is because the bioimpedance can be modelled by the Fricke-Morse model, which consist of a resistor in parallel with a capacitor and resistor in series. The implemented PCB can measure *DUT* magnitudes up to 1 k Ω and is determine the phase shift between the two PWM signals.

This work shows an important contribution towards a wearable continuous bioimpedance measurements system to monitor patient that suffer from heart failure. It has been shown that the presented design can measure the magnitude and phase that are required to determine the measured bioimpedance, and also reduce complexity of the measurements instrumentation.

Acknowledgements

This thesis has been a great and turbulent journey, especially in this extraordinary time. This thesis closes my chapter as a student, but I did not do it on my own.

First of all, I want to thank Vivo for supervising and supporting me during my thesis, even when the work and time difference in Canada came as an extra obstacle. I learned a lot from our discussions, and always enjoyed our the conversations outside of the office.

Thank you to everyone in the Bioelectronics group, especially Wouter. You always keep the group spirit up and you are always approachable for assistance. Also, I like to thank Cesc who helped me with a lot of difficult hurdles, and Merlin for great lunches and talks.

My PCB would not have been realized without the help of Ali and Ger, thank you. I like to thank also Esther and Marion for all the immediate help when needed, with great laughs included.

Lastly, I want to thank all my friends and family for the help and great moments we shared, with a special mention to Maike. Could not have done it without you.

*Brian Hanief Tufail Nanhekhan
Delft, August 2021*

Contents

List of Figures	ix
List of Tables	xi
1 Introduction	1
1.1 Background	1
1.1.1 Wearable Fluid Monitor.	1
1.1.2 Bioimpedance	2
1.1.3 Electrode Configuration	5
1.1.4 Measurement Instrumentation	5
1.2 Problem Statement.	6
1.3 Report Outline	7
2 Background	9
2.1 Wearable Bioimpedance Monitor	9
2.1.1 System Components	9
2.2 System Level Architecture	10
2.3 Transthoracic Bioimpedance Measurement.	11
2.3.1 Tissue Excitation	11
2.3.2 Bioimpedance Modeling	12
2.4 State-of-the-Art	12
2.4.1 Analog-to-Time Conversion	13
2.5 Thesis Objectives and Approach	15
3 System Design	17
3.1 Transthoracic Bioimpedance Monitor Design	17
3.1.1 Proposed System.	17
3.1.2 Requirements for Proposed Design	17
3.2 Circuit Design.	18
3.3 PWM Generator	19
3.3.1 Triangular Wave Generator Design	20
3.3.2 Non-ideal Circuit Operation	22
3.4 PCB Prototype	23
3.4.1 PCB Implementation	24
3.4.2 Excitation Circuit Implementation	24
4 Results	27
4.1 System Simulations	27
4.2 System Accuracy	27
4.2.1 Resistive DUT	28
4.2.2 Capacitive DUT.	29
4.2.3 Resistive and Capacitive DUT	30
5 Discussion	33
5.1 Discussion	33
5.1.1 Proposed PWM-based Measurement System	33
5.1.2 System Level Architecture	34
5.2 Conclusion and Contributions	34
5.3 Recommendations for Future Work	34
Bibliography	37

List of Figures

1.1	The Fricke-Morse electrical model of the bioimpedance. The resistance R_{ECF} and R_{ICF} represent the resistive path of the applied current inside and outside of the cell, respectively. The capacitance C_m quantifies the capacitive behavior of the cell membrane.	3
1.2	The frequency behavior of biological tissue. (a) At low frequencies the applied current only passes through the ECF. (b) At high frequencies the applied current passes through the ECF, ICF and the cell membrane. Figure adapted from [21].	3
1.3	The bioimpedance (Z) plot in the complex plane. R_0 represents the bioimpedance at zero frequency ($f = 0$) and R_∞ represents the bioimpedance at infinite frequency ($f = \infty$). Note that the vertical axis shows the negative imaginary part pointing up. Figure adapted from [21].	4
1.4	Two methods to measure thoracic bioimpedance: (a) Intrathoracic bioimpedance method [26]. (b) Transthoracic bioimpedance method [27].	4
1.5	Two common electrode configurations for measuring bioimpedance: (a) Two-electrode configuration (bipolar), driving and sensing are done via the same pair of electrodes (blue). (b) Four-electrode configuration (tetrapolar), the outer electrodes are the driving pair of electrodes (red) and the inner electrode pair are the sensing electrodes (blue). Figure adapted from [2].	5
1.6	Two conventional measurement instrumentation methods: (a) Self-balancing bridge based on an impedance bridge. Figure adapted from [40]. (b) Quadrature demodulation. Figure adapted from [21].	6
2.1	System level block diagram of a wearable bioimpedance monitor	10
2.2	System level architectures for wireless sensing systems. On the left side the blocks on-chip are depicted and on the right side the blocks at the receiver side are shown (off-chip). Data communication between the two sides is provide by wireless data transfer. (a) Analog-to-digital conversion (ADC). (b) Analog-to-time conversion (ATC). Adapted from [49].	11
2.3	Illustration of tissue excitation. Biological tissue is excited by an current I_{exc} and the bioimpedance Z_{bio} of the biological tissue allows for a voltage V_{sig} to be measured across the tissue.	11
2.4	Illustration of the excitation current I_{exc} and the measurable voltage V_{sig} with associated parameters.	12
2.5	System block diagram of an analog-to-time converter for measuring solely the amplitude of the signal at the sensing electrodes. Figure adapted from [51].	13
2.6	Analog-to-time conversion method that measures amplitude and phase: (a) System block diagram using three comparators. (b) Signal waveforms and pulses in the time domain. Figures adapted from [44].	14
2.7	A PWM-base analog-to-time conversion method. The measured voltage V_{in} is sampled by a triangular wave TW and converted to a PWM signal by a comparator. Figures adapted from [46].	15
3.1	Circuit diagram of the proposed PWM-based bioimpedance measurement instrumentation for a wearable bioimpedance monitor. The measured voltage V_{sig} and the reference voltage V_{ref} are converted to PWM signals $V_{PWM,s}$ and $V_{PWM,r}$, respectively.	19
3.2	Signals of the PWM generator. The input signals to the comparators $Comp_{PWM,s}$ and $Comp_{PWM,r}$ are sinusoidal signals represented by V_{sine} and the triangular wave signal V_{tri} . The PWM output signal of the comparators are illustrated by V_{PWM}	20

3.3	Block diagram of a first-order oscillator. (a) A basic first-order oscillator with each of the function represented by separate blocks. (b) A simplified representation with three of the functions, except for integration, combined in the Schmitt Trigger. Figure adapted from [65].	21
3.4	Local oscillator design of the implemented triangular wave generator. The Schmitt trigger circuit produces a square wave signal at the output $V_{out,st}$. The square wave is then integrated into a triangular wave V_{tri} and fed back to the Schmitt trigger.	22
3.5	Timing diagram of the triangular wave generator. (a) The output voltage $V_{out,st}$ of the Schmitt trigger. (b) The output triangular wave signal V_{tri} of the integrator circuit.	22
3.6	Circuit diagram of the implemented PCB.	23
3.7	Circuit diagram of the implemented excitation current source.	25
3.8	The prototype PCB	25
4.1	LTspice [®] simulation: the resulting signals in a single period $t_{exc} = 100 \mu s$ of the excitation current I_{exc} are shown. The load consist of a $DUT = 1 k\Omega$ and $R_{ref} = 500 \Omega$	28
4.2	LTspice [®] simulation: the output $V_{sig'}$ and $V_{ref'}$ of the INAs present a time delay of approximately $1.33 \mu s$ in comparison to the excitation current I_{exc}	28
4.3	Magnitude measurements on a pure resistive DUT : (A) the magnitude of $V_{PWM,s}$, $V_{sig'}$ and $V_{PWM,s}(meas)$ are evaluated and compared with the actual magnitude of the DUT . (B) The absolute magnitude error of the evaluated signals compared to the DUT . (C) The relative magnitude error of the evaluated signals compared to the DUT	29
4.4	Phase measurements on a pure resistive DUT : (A) The absolute phase shift of $V_{PWM,s}(meas)$ is evaluated with respect to $V_{PWM,r}(meas)$. (B) The relative phase shift of $V_{PWM,s}(meas)$ is evaluated with respect to $V_{PWM,r}(meas)$	30
4.5	Magnitude measurements on a pure capacitive DUT : (A) the magnitude of $V_{PWM,s}(meas)$ is evaluated and compared with the actual magnitude of the DUT . (B) The absolute magnitude error of $V_{PWM,s}(meas)$ compared to the DUT . (C) The relative magnitude error of $V_{PWM,s}(meas)$ compared to the DUT	30
4.6	Phase measurements on a pure capacitive DUT : (A) The phase shift of $V_{PWM,s}(meas)$ is evaluated with respect to $V_{PWM,r}(meas)$. (B) The relative phase error of $V_{PWM,s}(meas)$ is evaluated with respect to the expected phase shift of -90°	31
4.7	Magnitude measurements on a RC parallel combination as DUT : (A) the magnitude of $V_{PWM1}(meas)$ is evaluated and compared with the actual magnitude of the DUT . (B) The absolute magnitude error of $V_{PWM1}(meas)$ compared to the DUT . (C) The relative magnitude error of $V_{PWM1}(meas)$ compared to the DUT	31
4.8	Phase measurements on a RC parallel combination as DUT : (A) The absolute phase error of $V_{PWM1}(meas)$ is evaluated with respect to $V_{PWM,r}(meas)$, and compared to the calculated phase of the DUT . (B) The relative phase error of $V_{PWM1}(meas)$ is evaluated with respect to $V_{PWM,r}(meas)$, and compared to the calculated phase of the DUT	32

List of Tables

2.1	Excitation current parameters used in transthoracic bioimpedance measurements. . . .	11
2.2	Parameters for modelling of the bioimpedance.	12
2.3	Comparison of measurement instrumentation methods considering size, accuracy and easy of transmission	15
3.1	List of selected components for PCB implementation.	25

Introduction

Worldwide people suffer from chronic diseases such as diabetes, sleep apnea and congestive heart failure. Continuous monitoring of these patient can improve their quality of life. Nowadays, advancement in technology in the field of sensor development and system integration experienced a vast growth. Therefore, small-sized wearable health monitoring devices are now available, and these can monitor patients remotely in their everyday life. As a result, treatments of chronic diseases are improved, and costs for clinical healthcare is reduced. Said wearable devices are able to continuously monitor patient's blood glucose in case of diabetes, or sleeping patterns of patient who suffer from sleep apnea. Furthermore, patients who are diagnosed with congestive heart failure will benefit from a wearable monitoring device that detects exacerbation of the chronic disease [1]. Fluid congestion in the lungs, also called pulmonary edema, is a main indicator of heart deterioration. However, common procedures to monitor fluid congestion are limited to the symptomatic phase which occurs relatively late compared to pulmonary edema. Bioimpedance analysis is a promising technique which has been widely used to evaluate physiological changes in, for example, fluid volume and fat mass in the human body [2]. An advantage of bioimpedance analysis is that it can be measured noninvasively which makes said technique suitable for integration in wearable monitoring devices. Furthermore, bioimpedance measurement systems are less complex than clinical monitoring systems like an X-ray or MRI machine. Therefore, bioimpedance measurements can be performed remotely by patients without the need for clinical assistance. For several years, bioimpedance monitoring devices are already used to evaluate body composites like fluid volume, yet, the availability of a wearable bioimpedance fluid monitor for continuous monitoring is greatly limited. Bioimpedance fluid monitoring systems should be capable of observing the changes in the bioimpedance continuously [3]. In addition, the size of said systems are to be kept minimized for the comfort of the patients and the integration in a wearable monitoring device [4]. Conventional measurement instrumentation to evaluate the bioimpedance employ complex readout methods which increase power consumption and size of the instrumentation. A high power consumption puts a constraint on measuring the bioimpedance continuously. Moreover, said instrumentation require, in addition, signal processing methods which add to the power consumption and size of the whole monitoring system. In this thesis, the design of a bioimpedance monitor is presented that aims to reduce the complexity of the readout and decrease the power demand on processing by combining the readout instrumentation with the signal processing.

1.1. Background

1.1.1. Wearable Fluid Monitor

A wearable fluid monitor which uses the bioimpedance to keep track of the body's fluid level continuously requires knowledge of various concepts, such as pathology and technology. In order to understand the full functionality of said monitor these concept are explained consecutively.

Congestive Heart Failure

Congestive heart failure (CHF) is a pathophysiologic state of the heart in which the capability to pump blood around is reduced [5]. Acute exacerbation of the condition, also referred to as acute decom-

pensated heart failure (ADHF), is characterized by symptoms such as dyspnea, peripheral edema and fatigue [6]. However, patients who are diagnosed with ADHF suffer from recurrent hospitalization and increased mortality [7]. The reason for this is that the symptoms utilized by physicians as indicators for ADHF become apparent at a later stage than the preceding asymptomatic phase, associated with changes in hemodynamic and pulmonary fluid congestion [8]. For example, pulmonary edema occurs at 18 ± 10.1 days before the patient starts to experience the initial symptoms, such as dyspnea [9]. Therefore, using said asymptomatic indicators for exacerbation of the heart can prevent ADHF.

Monitoring Fluid Congestion

Pulmonary edema is one of the initial physiological changes that leads to ADHF [10]. Conventional methods of monitoring pulmonary edema require clinical examination, such as radiographic imaging of the chest (i.e. X-ray) or pulmonary capillary wedge pressure [11]. Said methods involve qualified physicians and hospitalized care which are time consuming and increase cost for healthcare [12]. There is a need for remote monitoring of CHF patients to reduce healthcare costs and improve their quality of life. Unfortunately, this has proven to be difficult [13]. In the last decade, telemonitoring has been used to monitor patients remotely outside of the hospital. Major drawbacks of this method is that it requires optimal compliance of the patients, and is mainly limited to the moment that the symptoms become apparent [14].

Another method is to use bioimpedance analysis (BIA) to evaluate physiological changes in body composites, such as fluid congestion. BIA employs bioimpedance measurements which are performed by applying an alternating electrical signal to biological tissue. Consequently, the tissue produces an alternating electrical response signal that is proportional to the bioimpedance of the tissue. Said bioimpedance is dependent on the frequency of the applied alternating electrical signal as well as the tissue composite.

Using BIA has several advantages over other fluid monitoring techniques. First of all, BIA employs a noninvasive technique to characterize tissue composite, such as the body fluid level. Moreover, BIA systems reduce complexity of the system's instrumentation compared to, for example, the magnetic coil of a MRI machine. Therefore, BIA systems do not demand for a qualified physician to perform the measurements, thus, making BIA suitable for remote usage and resulting in cost-effective healthcare. Second, advancement in technology has made it possible for techniques such as BIA to be integrated in miniaturized devices. Consequently, BIA can be integrated in a wearable fluid monitor to provide continuous monitoring of fluid levels. Therefore, fluid congestion in the lungs can be detected in an early stage and hospitalization can averted [15]. For this reason, this thesis will aim to use BIA as the technique to monitor pulmonary edema.

1.1.2. Bioimpedance

Bioimpedance, the impedance of biological tissue, can be evaluated by injecting an AC current in tissue and measuring the produced AC voltage across the tissue. This is the conventional approach of measuring the bioimpedance, also called the galvanostatic approach. Another approach, the potentiostatic approach, would be to apply an AC voltage to the tissue and measure the AC current through the tissue. However, this approach is less common in association with biological tissue [16]. The reason is that the galvanostatic approach allows for limiting the applied current which should comply with the maximum current injection allowed in the human body, according to safety regulations [17]. Accordingly, this thesis will aim to use the galvanostatic approach to measure the bioimpedance.

Bioimpedance is defined as a complex quantity which represents the opposition of conductive material, or a conductor, experienced by an alternating electrical current (AC). The bioimpedance Z can be measure by $Z = \frac{V}{I}$, where V is the voltage measured across the conductor and I the current circulating through the conductor. As mentioned before, the bioimpedance is complex and dependent on the tissue composite as well as the frequency of the applied current (1.1). The real part R represents the resistance caused by the fluids in the body, and the imaginary part is given by the reactance X_c which correlates with the capacitance of the cell membrane [18].

$$Z = R + jX_c \quad (1.1)$$

In order to gain a better understanding about the bioimpedance and the influence of the composite of the tissue, various models are established. One of the initial models, the Fricke-Morse model, state that

biological tissue consists mostly of cells [19]. These cells are surrounded by extracellular fluids (ECF), and they contain intracellular fluids (ICF). Due to the ions dissolved in these fluids a conductive path is provided for an applied current and, hence, the current will experience resistance in the fluids outside and inside of the cell (R_{ECF} and R_{ICF} , respectively). The cell membrane, which separates the ICF and ECF, is made of two conductive outer layers with a nonconductive material between them, making the cell membrane to resemble a capacitor (C_m). As a result, the Fricke-Morse model for biological tissue impedance is illustrated in Fig. 1.1.

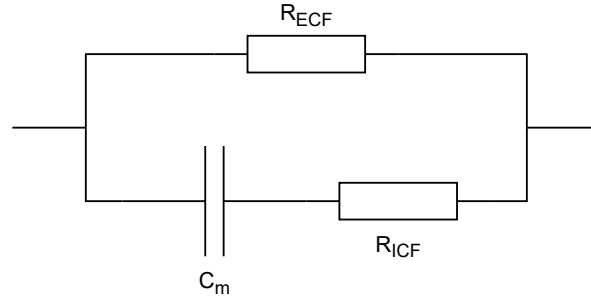


Figure 1.1: The Fricke-Morse electrical model of the bioimpedance. The resistance R_{ECF} and R_{ICF} represent the resistive path of the applied current inside and outside of the cell, respectively. The capacitance C_m quantifies the capacitive behavior of the cell membrane.

The frequency-dependent behavior of biological tissue is depicted in Fig. 1.2, which complies with the electrical model of the bioimpedance shown previously in Fig. 1.1. At low frequencies (<1 kHz) the applied current passes only through the ECF due to the capacitive behavior of the cell membrane. When higher frequencies are applied (>100 kHz), the current is passing through the cell membrane as well as the ICF [20].

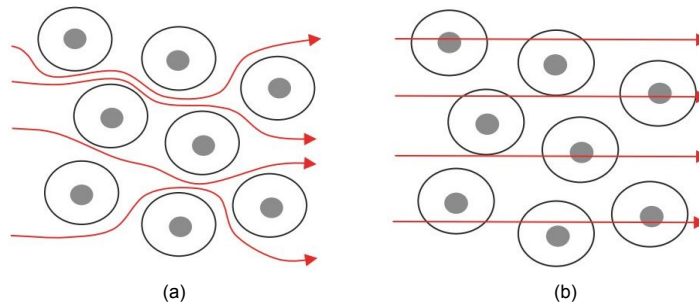


Figure 1.2: The frequency behavior of biological tissue. (a) At low frequencies the applied current only passes through the ECF. (b) At high frequencies the applied current passes through the ECF, ICF and the cell membrane. Figure adapted from [21].

Therefore, the expression of the Fricke-Morse model can be simplified and expressed as in (1.2), where $R_0 = R_{ECF}$, $R_\infty = R_{ECF} \parallel R_{ICF}$, $\tau = (R_{ECF} + R_{ICF}) \cdot C_m$, and f is the frequency of the applied current.

$$Z(f) = R_\infty + \frac{R_0 - R_\infty}{1 + j \cdot 2\pi f \tau} \quad (1.2)$$

The resistance R_0 represents the bioimpedance at zero frequency ($f = 0$), or DC, and R_∞ represents the bioimpedance at infinite frequency ($f = \infty$). Plotting the bioimpedance from $f = 0$ to $f = \infty$ in the complex plane resembles a semicircle that moves counterclockwise with the increasing frequency, as depicted in Fig. 1.3. Considering the characteristics of said plot, the bioimpedance can be derived with the help of (1.2).

Studies have shown more accurate, yet, more complex models to derive the bioimpedance. A commonly used model is the Cole-Cole model [22] which generalizes the expression and takes into account nonidealities assumed in (1.2). A couple of said nonidealities are that the capacitor does not

behave as an ideal capacitor, and the heterogeneity of cells' structures [23]. Nevertheless, the Cole-Cole model is difficult to interpret and complicates the employment of the model [24]. Therefore, for simplicity, the Fricke-Morse model is assumed in the rest of the thesis.

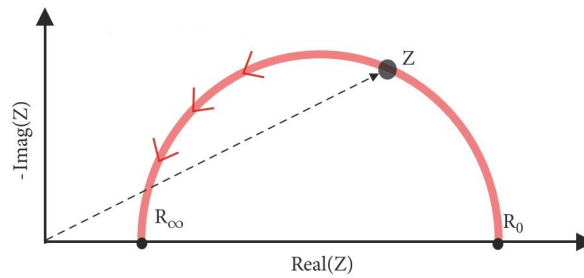


Figure 1.3: The bioimpedance (Z) plot in the complex plane. R_0 represents the bioimpedance at zero frequency ($f = 0$) and R_∞ represents the bioimpedance at infinite frequency ($f = \infty$). Note that the vertical axis shows the negative imaginary part pointing up. Figure adapted from [21].

Intrathoracic vs Transthoracic Bioimpedance

Pulmonary edema is a prominent indicator for decompensation of the heart and measuring fluid congestion in the thorax by means of bioimpedance helps to observe it. Applying an AC current to the thorax when fluid is congested in the lungs will allow for the current to conduct better. The reason is that the accumulated intrathoracic fluid provides a better conductive path, resulting in a decreased bioimpedance. The thoracic bioimpedance can be measured with two conventional methods: from the inside of the body (intrathoracic) or from the outside of the body (transthoracic) [9].

Intrathoracic bioimpedance is measured by means of a implantable device, such as an implantable cardioverter defibrillator (ICD) or cardiac resynchronisation therapy defibrillator (CRT-D) [25]. An additional lead is added to said devices and it is implanted in the heart's right ventricle (RV). The intrathoracic bioimpedance is measured between the lead and the device casing that is implanted in the left pectoral region, illustrated in Fig. 1.4a. The other method, the transthoracic bioimpedance method, is executed externally by placing surface electrodes on the thorax, depicted in Fig. 1.4b. A dedicated bioimpedance device injects the current and measures the developed voltage, via the surface electrodes [26].

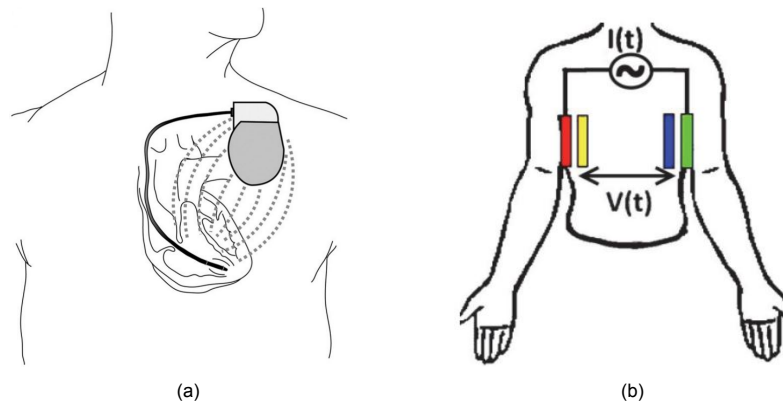


Figure 1.4: Two methods to measure thoracic bioimpedance: (a) Intrathoracic bioimpedance method [26]. (b) Transthoracic bioimpedance method [27].

An advantage of the transthoracic method is that it can be applied noninvasively and the bioimpedance can be measured immediately. Whereas, the intrathoracic method requires an invasive surgery, and recovery time before measurements can be executed [25]. In addition, only a few HF patients are in immediate need of an implant [28]. Therefore, only a small group of patients are eligible for an implantable bioimpedance device for intrathoracic bioimpedance measurements. A considerable drawback of the transthoracic method and the use of surface electrodes is the repeatability and reliability of the measurements [29]. Commonly used adhesive electrodes have poor repeatability due to the need for correct placement of the electrodes. In addition, they can cause skin irritation due to the

adhesive gel [30]. Studies have been conducted to come up with a solution such as different kind of materials for the electrodes [31], and textile-integrated electrodes [32]. Considering the above, this thesis will focus on the transthoracic bioimpedance method.

1.1.3. Electrode Configuration

In order to measure transthoracic bioimpedance using the galvanostatic approach at least two electrodes are needed. Current injection is applied by a pair of electrodes, the driving electrodes. Similarly, the measured voltage is evaluated by a pair of electrodes as well, the sensing electrodes. Bioimpedance measurements are performed by employing two common electrode configurations: bipolar and tetrapolar, illustrated in Fig. 1.5. The former is implemented such that the driving and the sensing electrodes share the same pair of electrodes. The advantage of this configuration is that only one pair of electrodes is needed as well as less circuitry [33]. The tetrapolar configuration employs two separate pairs of electrodes for driving and sensing. Generally, an instrumentation amplifier is used to measure the voltage across the sensing electrodes. An important advantage of tetrapolar over bipolar when performing BIA is the effect of the contact impedance on the measured voltage. Injecting a current into the body creates a contact impedance at the electrode-tissue interface. Considering the bipolar configuration, said contact impedance is measured in addition to the bioimpedance. The contact impedance can be several magnitudes higher than the measured bioimpedance, hence, causing insensitivity for measuring the bioimpedance [34]. Whereas in the tetrapolar configuration, the instrumentation amplifier connected to the sensing electrodes has a high input impedance. Therefore, almost no current will flow into the sensing electrodes and the contact impedance can be neglected. Other electrode configurations employed in, for example, bioimpedance tomography [35], are not considered in this thesis. Therefore, this thesis will examine transthoracic bioimpedance measurements employing the tetrapolar configuration.

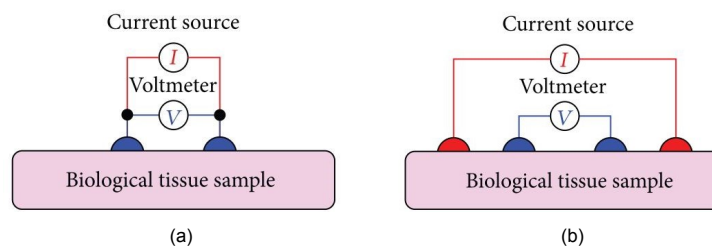


Figure 1.5: Two common electrode configurations for measuring bioimpedance: (a) Two-electrode configuration (bipolar), driving and sensing are done via the same pair of electrodes (blue). (b) Four-electrode configuration (tetrapolar), the outer electrodes are the driving pair of electrodes (red) and the inner electrode pair are the sensing electrodes (blue). Figure adapted from [2].

1.1.4. Measurement Instrumentation

Two conventional instrumentation methods can be distinguished regarding the measurement of the bioimpedance: the impedance bridge and quadrature demodulation. The impedance bridge method employs the practical implementation of a self-balancing bridge structure depicted in Fig. 1.6a. The excitation voltage V_0 is applied to the tissue with unknown bioimpedance Z_x resulting in a current I_x to flow through Z_x . The function of the null detector connected to node G is to match the current I_f with I_x by adjusting the magnitude and phase of V_f such that the voltage at node G is balanced to zero. Afterwards, the bioimpedance can be derived by means of the known resistance R_f according to $Z_x = R_f \frac{V_f}{V_0}$. Generally, the impedance bridge method was considered a prominent method due to the high accuracy and resolution of the measurements. However, the quadrature demodulation methods has gained an advantage over the impedance bridge method regarding accuracy, speed and simplicity [36]. The main reason is that the impedance bridge method is time-consuming due to the balancing of the bridge impedance, which makes it less suitable for measurements where the bioimpedance changes over time [37]. Moreover, the impedance bridge method employs a bipolar electrode configuration and commonly a potentiostatic approach [38]. As mentioned previously in this section, said concepts are not suited for measuring the bioimpedance in the human body. Nowadays, quadrature demodulation is commonly used for bioimpedance measurement and is based on the multiplication of the measured voltage with two orthogonal signals derived from the excitation signal: in-phase (0°) and

quadrature (90°), as illustrated in Fig. 1.6b. Subsequently, the multiplied signals are low-pass filtered, resulting in the real (phase) component and the complex (quadrature) component of the bioimpedance. Generally, the components of the bioimpedance are digitized and processed digitally to obtain the final bioimpedance. Despite that quadrature demodulation is applicable for bioimpedance measurement of the human body due to speed and accuracy, it comes at the cost of complexity and power consumption. Namely, in generating the orthogonal signals, mismatch should be avoided to prevent large phase errors. Alternatively, compensation techniques could be applied, but said techniques add to the complexity and power consumption of the system [39].

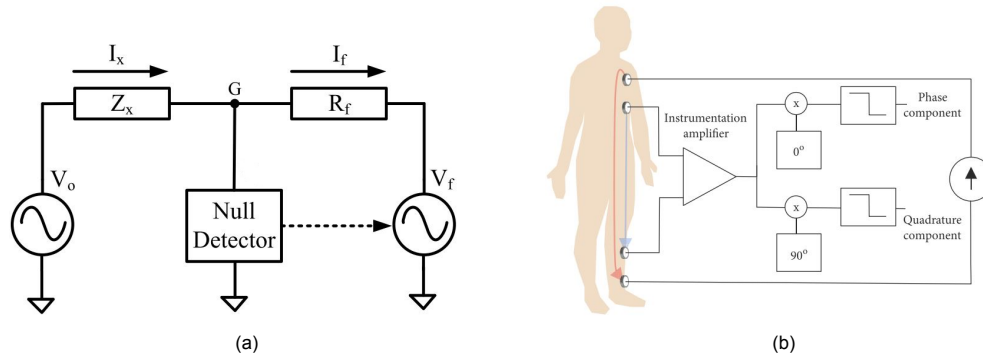


Figure 1.6: Two conventional measurement instrumentation methods: (a) Self-balancing bridge based on an impedance bridge. Figure adapted from [40]. (b) Quadrature demodulation. Figure adapted from [21].

1.2. Problem Statement

Transthoracic bioimpedance measurements provide a noninvasive method to realize remote health monitoring of patients that suffer from CHF. However, designing said monitoring system imposes challenges on the measurement instrumentation. First of all, the system should be capable of continuous monitoring the changes in thoracic bioimpedance of patients. When fluid accumulates in the lungs, the associated thoracic bioimpedance will decrease. This change in bioimpedance, also called the dynamic bioimpedance, is a few decades smaller compared to the static bioimpedance caused by tissue such as bone and muscles [41]. Measuring the absolute bioimpedance would mainly consist of the static bioimpedance. Therefore, the relative bioimpedance should be measured which has to be done continuously to keep track of the changes. As a result, the power consumption of the monitoring system should be minimized to realize long-term continuous monitoring without the need to change batteries on a daily basis.

Second, remote monitoring of the transthoracic bioimpedance involves patient to self-manage the measurement. In order to ensure accurate and reliable measurements, the monitoring system should be easy-to-use and unobtrusive for patients [42]. Studies have shown methods to improve the use of bioimpedance monitoring systems by patients [43]. Smaller-sized systems would ease the integration of said systems in, for example, textile vests, or bioimpedance bands around the thorax. Therefore, the size of the transthoracic bioimpedance monitoring system should be minimized.

Finally, instrumentation methods to measure bioimpedance should be low-power and have reduced complexity to ensure small and reliable systems. Moreover, remote usage of a bioimpedance monitor demands a wireless connection between the device and the physician [43]. When designing the measurement instrumentation, methods should be considered that allow for low-power wireless communication which minimizes the additional complexity of said wireless communication technique. In light of all the above, the research question of the thesis is formulated as follows:

How can the transthoracic bioimpedance be monitored remotely to provide continuous, accurate and reliable measurements in order to ensure self-management and comfort for patients with congestive heart failure?

1.3. Report Outline

The rest of this thesis report is organized as follows: first, a literature review is conducted on the background of bioimpedance measurement systems and state-of-the-art bioimpedance measurements instrumentation are presented in [Chapter 2](#). Subsequently, the design and printed circuit board (PCB) implementation of the proposed system is discussed in [Chapter 3](#). Then, simulations and measurements on the PCB are performed to validate the system in [Chapter 4](#). Lastly, [Chapter 5](#) present a discussion and conclusion of the work in this thesis and gives recommendations for future work.

2

Background

2.1. Wearable Bioimpedance Monitor

2.1.1. System Components

In [Fig. 2.1](#), a system-level block diagram of the fundamental components in a wearable bioimpedance monitor is depicted. Depending on the application and the associated requirements, additional blocks could be added or removed to the system. Firstly, the power management block ensures that the system is powered so that all the blocks are functional correctly. For a battery-powered device, this block monitors the voltage level of the battery and regulate the voltages to the rest of the system. As an alternative to a battery-powered system, an inductive link that is commonly employed in implantable bioimpedance systems, which have a similar system level design, can provide power to the system. Additionally, data telemetry can be facilitated through the same inductive link [\[44\]](#).

The measurement instrumentation block consists of the excitation circuit and the readout. The excitation is applied to the human body by a pair of driving electrodes and, subsequently, the response voltage is measured by the sensing electrodes. The excitation circuit applies a current to the human body according to the parameters stored on the device. Commonly, the excitation current is sinusoidal and derived from a voltage-controlled current source (VCCS) that is controlled by a driving voltage. Generating a pure analog sinusoidal voltage to drive the VCCS requests a high power consumption. Alternatively, the driving voltage can generated digitally and converted to the analog domain by. Studies have also shown other types of excitation signals. A square wave signal can be generated low-power, however, the additional harmonics causes significant errors. Furthermore, a pseudo random signal avoids additional harmonics, although, it adds complexity to the system [\[45\]](#). This thesis will assume sinusoidal current excitation. Considering the readout block, the voltage as response to the current injection is measured by the sensing electrodes connected to the input of an instrumentation amplifier (INA). The INA provides a high-impedance at the input and amplifies the measured voltage in order to increase the resolution.

In the subsequent control block, the analog data at the output of the INA is conditioned and processed by the processing unit. The data is processed conventionally in the digital domain. However, this processing can also be done in the analog or time domain. Depending on the type of data processing, the data can be conditioned by converting it to the correct domain. Moreover, analog signals are susceptible to noise. Therefore, the analog signal is conventionally converted to the digital domain by an analog-to-digital converter (ADC). Subsequently, the digital data can be processed directly by a digital signal processor (DSP). Time signals provide similar robustness against noise and interference as digital signals [\[46\]](#). However, the conversion to the time domain requires less complex circuitry. Still, time signals are commonly processed in the digital domain, but this signals can also be processed in the time domain components such as logic gates [\[47\]](#). Furthermore, the control block also provides the system of telemetry. The processed data is forwarded to the data storage for temporal storage, or to the wireless unit. Depending on the type of wireless data transfer (WDT), for example radio frequency (RF) or ultra-wideband (UWB), the wireless unit provides encoding and decoding of data that is to be transmitted or received, respectively. In addition, the wireless unit consist of a transceiver which facilitates data telemetry. The transceiver transmits the measured bioimpedance data from the monitor to

a device that operates as a hub, such as a mobile phone or a PDA. Next, the measured data is transmitted to a remote database where the physician can access the data [48]. Moreover, the transceiver facilitates that the device to receive different parameters for the excitation circuit on the advice of the physician. The parameters are stored in the data storage and forwarded to the excitation circuit.

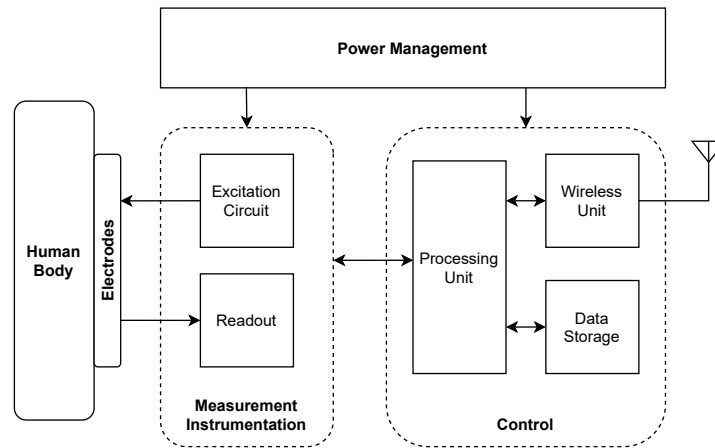


Figure 2.1: System level block diagram of a wearable bioimpedance monitor

2.2. System Level Architecture

A wearable bioimpedance monitor is an implementation of a wireless sensing system. Considering wireless sensing systems, various system level architectures can be distinguished regarding the control block depending on the application. Each type of system level architectures employs a distinct integration of the system level blocks and the interconnections between this block in the entire system.

Traditionally, wireless sensing systems consist of Nyquist-rate sampling by an ADC which samples the analog data from the readout to ensure immunity from noise and interference [49], and to facilitate digital processing. The processing of digital data can be executed by a DSP and transmitted via a radio frequency transmitter (RF TX). Such a system level architecture approach is illustrated in Section 2.2. An advantage of this approach is that the amount of raw digital data is reduced which decreased the power demand of the wireless unit. However, reduction of the digital data might result in loss of useful information [50]. In addition, implementing a DPS on-chip increases the complexity of the system. To overcome the disadvantages, the DSP can be moved to the receiver side (off-chip). As a result, high-resolution digital data is provides and the amount of system blocks is reduced. However, the disadvantage is that an ADC produces a high amount of raw data to be transmitted wirelessly which in turn increasing the load on the wireless unit [49]. Therefore, careful consideration should be made in choosing the system level architecture approach with a trade-off between complexity and resolution.

An alternative system level architecture can be implemented by converting the measured analog signal to a time domain signal, such as a square wave or a pulse-width modulated (PWM) signal, by an analog-to-time converter (ATC). The advantage of this approach compared to the ADC approach is that the complexity of the converter is reduced. Commonly, the time domain signals are still converted by means of a time-to-digital converter (TDC) and processed in the digital domain. However, time signals can be transmitted wirelessly by the same type of WDT methods as digital signals. Therefore, the TDC can be moved to the receiver side and time signals can be transmitted there for processing, as illustrated in Section 2.2. Although, some applications require processing to be performed on-chip. In that case, the ATC approach would be disadvantageous since an extra step is required to convert the analog signal to the digital done. However, time signals are characterized by a high and low value. Consequently, processing in the time domain is possible as well by simple logic gates [47]. As previously mentioned, following a system level architecture approach involving ATC depend on the requirements of the system, similar to the ADC approach. A trade-off should be considered between complexity and data processing.

ATC can be perform at lower power due to the simplicity of the implementation [51]. Moreover, this approach is be advantageous, because the TDC is moved to the receiver side which saves area and

power [52]. However, the ATC approach is not suitable for application that require the time domain data to be processed directly, for instance, on the receiver side. The reason for this is that the data in the time domain should first be converted to the digital domain to be processed by a DSP or a computer.

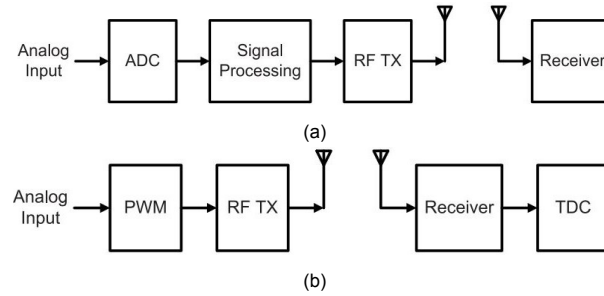


Figure 2.2: System level architectures for wireless sensing systems. On the left side the blocks on-chip are depicted and on the right side the blocks at the receiver side are shown (off-chip). Data communication between the two sides is provide by wireless data transfer. (a) Analog-to-digital conversion (ADC). (b) Analog-to-time conversion (ATC). Adapted from [49].

2.3. Transthoracic Bioimpedance Measurement

2.3.1. Tissue Excitation

The most commonly used excitation current waveform is a sine wave. When the excitation current (I_{exc}) is applied to biological tissue, such as the human body, a measurable voltage (V_{sig}) is developed across the tissue as a result of the bioimpedance (Z_{bio}), as depicted in Fig. 2.3. The excitation current can be expressed as $I_{exc} = I_0 \cdot \sin(2\pi f_{exc}t)$, and the measured voltage can be expressed as $V_{sig} = V_0 \cdot \sin(2\pi f_{exc}t + \phi_{ps})$, as illustrated in Fig. 2.4. The amplitude of I_{exc} and V_{meas} are represented by I_0 and V_0 , respectively, the frequency f_{exc} of both signals is equal to the frequency of I_{exc} , and the phase shift ϕ_{ps} in V_{meas} is caused by the Z_{bio} . Furthermore, Z_{bio} is a complex quantity that can be represented by a magnitude $Z_0 = \frac{V_0}{I_0}$, and a phase angle ϕ_{ps} . Therefore, the bioimpedance is given by:

$$Z_{bio} = Z_0 \cdot e^{j\phi t} \quad (2.1)$$

The parameters I_0 and f_{exc} determine the excitation current. First of all, the amplitude I_0 should comply with safety regulations. The amplitude should be limited to a maximum of $1 \mu\text{A}$ below 100 Hz, $100 \mu\text{A}$ above 10 kHz and in between I_0 can be equal to $100 \cdot f_{exc} \mu\text{A}$ [53]. Second, studies have mostly mentioned a frequency range of 1 kHz – 1 MHz [31, 53, 54]. In the range the physiological changes such as change in body fluids can be observed most effectively. The parameters regarding the excitation current are summarized in Table 2.1.

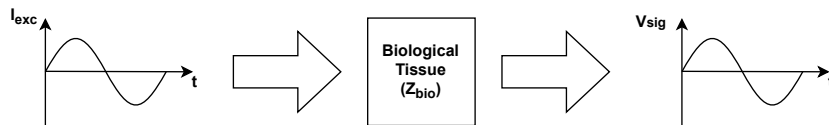


Figure 2.3: Illustration of tissue excitation. Biological tissue is excited by an current I_{exc} and the bioimpedance Z_{bio} of the biological tissue allows for a voltage V_{sig} to be measured across the tissue.

Table 2.1: Excitation current parameters used in transthoracic bioimpedance measurements.

Parameter	Value
Waveform	Sine
I_0	$1 \mu\text{A} - 100 \mu\text{A}$
f_{exc}	$1 \text{ kHz} - 1 \text{ MHz}$

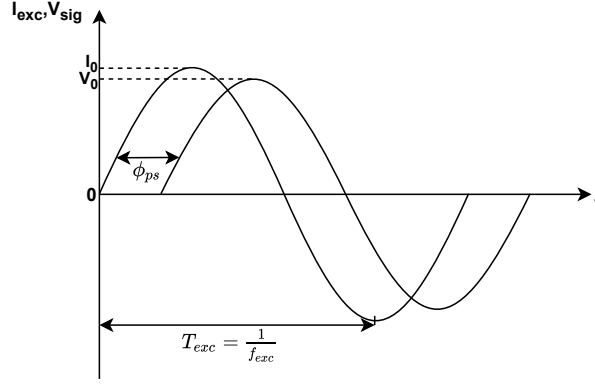


Figure 2.4: Illustration of the excitation current I_{exc} and the measurable voltage V_{sig} with associated parameters.

2.3.2. Bioimpedance Modeling

As mentioned in [Section 1.1.3](#), the electrode configuration used in bioimpedance measurements can contribute to the modeling of the total bioimpedance. The electrode-tissue interface can be modelled by an equivalent electrical circuit representation when the electrode is attached to the body [55]. In case of a current passing through the electrode, the result will be a voltage drop across the interface. However, a tetrapolar configuration is commonly used for bioimpedance measurement and the configuration minimizes the current that passes through the sensing electrodes to <200 pA [56]. Furthermore, the assumption will be made that the impedance of the current source will be much greater than the electrode impedance, and no mismatch is present between the electrode impedance of both the sensing electrodes. Therefore, the voltage drop across the electrode-tissue interface, as a result of the contact impedance, can be neglected.

In [Fig. 1.1](#) the electrical model of the bioimpedance was shown. This model will be used to establish the requirements of the system and for the initial tests. Therefore, the typical values for the thoracic bioimpedance of a human male are assumed. Furthermore, the bioimpedance comprises a static (Z_b) and a dynamic (ΔZ_{bio}) bioimpedance. The latter is of interest to measure the change in the thoracic fluid and is in the range of $m\Omega$, whereas Z_b is in the range of Ω . Based on the research done employing the electrical model of the bioimpedance [56] and measuring the change in fluid volume in the thorax [27, 57], various parameters with typical values can be established, depicted in [Table 2.2](#). The parameters of the excitation and the bioimpedance model will be used to set up the requirements for designing readout of the system. The requirements are, for example, input voltage range and bandwidth.

Table 2.2: Parameters for modelling of the bioimpedance.

Parameter	Typical Value
R_{ECF}	34.8Ω
R_{ICF}	33Ω
C_m	33 nF
Z_b	$1 \Omega - 1 \text{ k}\Omega$
ΔZ_{bio}	$10 \text{ m}\Omega - 1000 \text{ m}\Omega$

2.4. State-of-the-Art

In [53], a measurement system architecture is presented which immediately digitizes the measured signal at the readout by means of an ADC. Subsequently, the bioimpedance is extracted from the measured digital data off-chip. In order to extract the bioimpedance, the measured data is synchronized with the excitation signal that is, likewise, generated off-chip in the digital domain. This approach benefits from less components on-chip which reduces size and power. However, as mentioned in [Section 2.2](#), integration of this approach in a wearable bioimpedance monitor would increase the load on the wireless unit by the excessive raw ADC data.

In order to reduce the raw data, a pre-processing method is employed in [58]. The conventionally used quadrature demodulation approach is taken to pre-process the measured data in the analog domain. As a result, only the real and imaginary part of the measured bioimpedance are converted by the ADC. Furthermore, a sensing resistor of a known value is used in series with the bioimpedance. The voltage across the resistor is used to generate the two orthogonal signals that are multiplied with the measured signal. Therefore, synchronizing the measured signal with the excitation signal. Although this approach reduces the load on the wireless unit, and therefore the power consumption, higher order analog filters are needed in addition to a high-speed ADC [44]. The reason for this is to ensure good signal-to-noise-ratio (SNR) and adequate processing time. However, this implementation increases the power consumption again as well as the complexity. In addition, the ADC and the transmission of digital signals are power demanding functions for wireless transmission [59]. Therefore, the proper format of the measured data can contribute to the employment of a low-power wireless unit. Also, processing and filtering of the measured data will result in loss of information. As a result, reconstruction of the original measured signal becomes more challenging.

2.4.1. Analog-to-Time Conversion

As mentioned in Section 2.2, an alternative format of the measured signal is time domain signals. In [51] the measured signal is converted to the time domain by a comparator. The measured signal is compared with a reference signal that has a known phase which is derived from the excitation source, as illustrated by comparator B in Fig. 2.5. In addition, that same reference signal is compared with ground by comparator A. The sensing unit employs a multiplexer to select the sensing electrode pair, and an instrumentation amplifier which output is connected to comparator B. The approach used in this system is solely to measure the amplitude of the measured signal, and not the phase. Considering the output signals of the comparators, the rising and falling edge of capture B represent the moment the inputs of comparator B are equal. The edges of Capture A indicate the zero crossings of the reference signal. Consequently, the time difference between the edges of capture A and B relates to the amplitude of the measured signal. Accordingly, the time between a rising edge of Capture A and one of Capture B indicates the time it takes from a zero crossing to the moment when the measured and the reference signal are equal. As a result, the amplitude of the measured signal can be derived from the reference signal. The presented approach has several advantages over the ADC approach. First of all, no external clock is needed to convert the measured signal to the time domain. Instead, conversion is triggered when the analog inputs cross a reference. Moreover, only two comparators are needed to implement the converter which significantly reduce the complexity of the converter [60]. A disadvantage of this approach is that the amplitude can be determined exclusively. The phase of the measured signal is essential for deriving the bioimpedance.

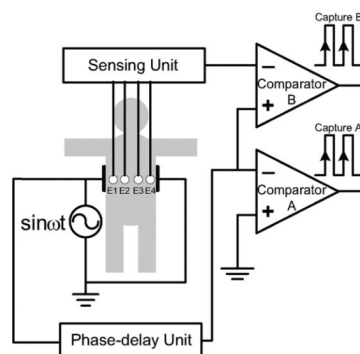


Figure 2.5: System block diagram of an analog-to-time converter for measuring solely the amplitude of the signal at the sensing electrodes. Figure adapted from [51].

In [44], a third comparator is added to a similar system design to extract the phase of the measured signal as well. A block diagram of the system and the associated signals are depicted in Fig. 2.6. The third additional comparator is represented by the top comparator in Fig. 2.6a with output $VP1$. The excitation current through electrodes $E1$ and $E2$ is generated by a VCCS from a reference voltage source V_{ref} . Electrodes $E3$ and $E4$ are the sensing electrode which measure the response voltage V_m through an instrumentation amplifier (IA). In Fig. 2.6b the pulses shown represent the rising edge

of the output signal of the comparators. Firstly, the phase difference ϕ between the V_{ref} and V_m are indicated by time T_1 and T_2 , and can be calculated by: $\phi = 2\pi \cdot \frac{T_1 - T_2}{(1/f_{exc})}$, where f_{exc} is the frequency of V_{ref} . Furthermore, the amplitude of V_m can be determined by means of signal $VP3$. For $V_{ref} = A_{ref} \cdot \sin(2\pi f_{exc} \cdot t)$ and $V_m = A_m \cdot \sin(2\pi f_{exc} \cdot t + \phi)$, where A_m is the unknown amplitude. At $t = T_3$, the measured voltage $V_m = V_{ref}$, and as a result, $V_{m,T_3} = A_{ref} \cdot \sin[2\pi f_{exc} \cdot (T_3 - T_1)]$. Subsequently, the amplitude A_m can be calculated by $A_m = \frac{V_{m,T_3}}{\sin[2\pi f_{exc} \cdot (T_3 - T_2)]}$. This method shows the advantage of measuring the amplitude as well as the phase difference of the measured voltage. Accordingly, the magnitude and phase of the bioimpedance can be derived. Furthermore, the time signals generated as an output by this method contribute to the employment of low-power transmission techniques, such as passive phase-shift keying (PPSK) [44]. Although, the presented ATC methods lack the preservation of the original measured signal which result in the loss of information.

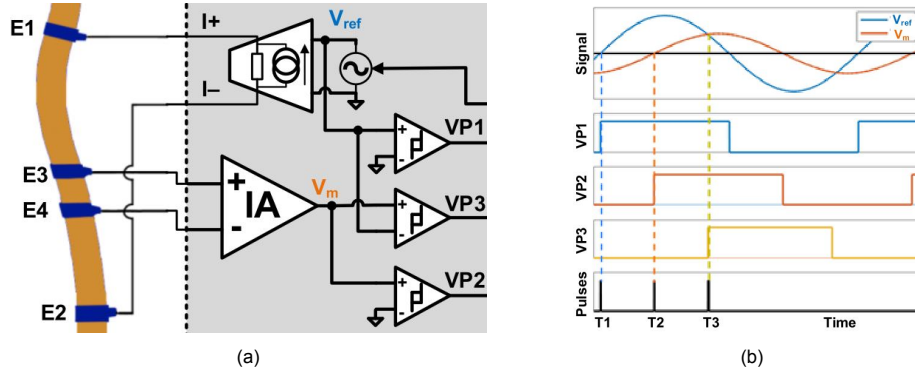


Figure 2.6: Analog-to-time conversion method that measures amplitude and phase: (a) System block diagram using three comparators. (b) Signal waveforms and pulses in the time domain. Figures adapted from [44].

The aforementioned ATC methods modulate the measured analog signal to square wave time signals. Consequently, at least two comparators are required to determine the amplitude of the signal measured at the sensing electrode. Alternatively, pulse modulation techniques can be used to modulate the voltage of the measured signal into the time signal. A pulse width modulation (PWM) approach is presented in [46] which uses the variable width of a time signal to represent the voltage of the measured analog signal. In Fig. 2.7, a system block diagram of a PWM signal generator circuit is shown, as well as the input and output signals. The triangular wave signal TW is used as an carrier signal which modulates the voltage V_{in} into the pulse width, by varying the duty-cycle, of the PWM output provides by the comparator. When $TW < V_{in}$ the output is high. Conversely, when $TW > V_{sig}$ the PWM output is low. The frequency of the PWM output is equal to that of the triangular wave. To demodulate the original analog voltage from the PWM signal, for example, the PWM signal can be low-pass filtered [61]. Alternatively, a TDC can be employed and reconstruction can be done in the digital domain. Lastly, the PWM signal is transmitted via frequency shift keying (FSK) and processed on the receiver side. The main advantage of the PWM approach is that the complete measured analog voltage is modulated in the PWM time signal. In order to reconstruct the original voltage, the sampling carrier triangular wave should provide Nyquist-rate sampling [62]. Moreover, the presented approach employs a reference signal that is also converted to a PWM signal and transmitted in order to mark the start and end of a measurement. Lastly, the triangular wave generator (TWG) should be designed with care, since it directly affects the noise, accuracy and resolution of the system [63].

The time signals generated by an ATC do not directly represent the parameters associated with the measured bioimpedance, such as magnitude and phase. Generally, this time signals should be demodulated for additional processing to derive the parameters of the bioimpedance. First of all, the most conventional method to process time signals on the receiver side would be in the digital domain. Therefore, the received time signals are demodulated by a TDC. The pulse width of the time pulses are counted and digitized for processing in the digital domain [46, 47, 60]. Digital signal processing benefits from fast and accurate data processing. Alternatively, time signals can be pre-processed by simple low-power logic blocks [64]. This approach could be implemented on-chip to, for example, reduce the amount of data that is transmitted. However, again data will be lost as explained in Section 2.2.

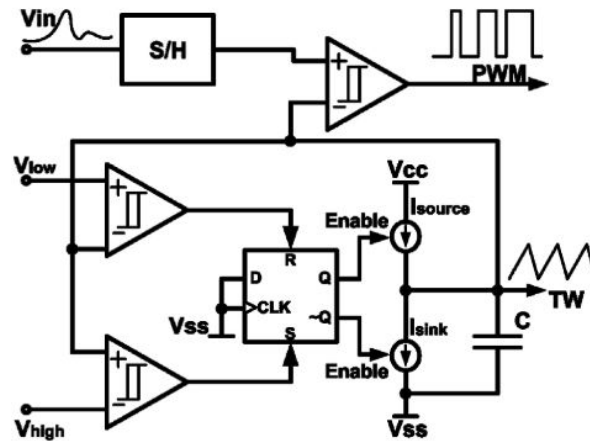


Figure 2.7: A PWM-base analog-to-time conversion method. The measured voltage V_{in} is sampled by a triangular wave TW and converted to a PWM signal by a comparator. Figures adapted from [46]

In this state-of-the-art section, various measurement instrumentation methods were discussed and a comparison between them is presented in Table 2.3. Power consumption in this table takes into account the power requires for the instrumentation method as well as the the load on the wireless unit. Furthermore, size represents the complexity of the method. The accuracy considers the amount of information of the original analog signal that can be extracted from the converted output signal. Lastly, the data format relates to the easy of transmission of the converted data which affects the type of transmission that can be implemented.

Table 2.3: Comparison of measurement instrumentation methods considering size, accuracy and easy of transmission

Instrumentation Method*	Power Consumption	Size	Accuracy	Data Format	Implemented in
ADC DC	-	+	++	-	[53]
ADC IC	-	-	+	+	[58]
ATC SW	++	++	-	++	[44, 51]
ATC PWM	+	+	++	++	[46]

*ADC = analog-to-digital conversion, ATC = analog-to-time conversion, DC = direct conversion, IC = indirect conversion, SW = square wave, PWM = pulse width modulation.

2.5. Thesis Objectives and Approach

The literature review presented in this chapter leads to the following hypothesis: the use of analog-to-time conversion employing pulse width modulation could lead to continuous, accurate and reliable measurements of the transthoracic bioimpedance. This approach is promising on basis of the subsequent reasons:

- Analog-to-time conversion allows for time signals that have the same robustness as digital signals against noise and interference.
- Analog-to-time conversion employs a clockless approach, accordingly, no high frequency clock is required on-chip.
- Pulse width modulation preserves the measured analog signal in the variable pulse width of the time signal.
- Time signals can be transmitted more effectively than digital signals.
- Time-to-digital conversion on the receiver side can be performed with ease by measuring the pulse width of the received time signal.

The objective of this thesis is to design a system that employs ATC in combination with PWM. Furthermore, a reference signal should be generated by the system as well and converted to a PWM signal in order to derive the magnitude and phase of the measured bioimpedance.

3

System Design

This chapter describes the design process of the proposed bioimpedance measurement instrumentation. First, system level design considerations for the wearable bioimpedance monitor are covered. Based on these considerations, a bioimpedance readout is designed capable of converting measured analog signals to a pulse width modulated (PWM) signal while additionally generating a reference signal. Finally, the circuit is simulated and implemented on a printed circuit board (PCB) for validation.

3.1. Transthoracic Bioimpedance Monitor Design

3.1.1. Proposed System

Based on the literature presented in [Chapter 2](#), the approach that is chosen for the measurement instrumentation of a wearable transthoracic bioimpedance monitor employs PWM-based analog-to-time conversion (ATC) [46]. The approach converts the voltage of the measured analog signal to a PWM time-based signal from which the magnitude of the analog voltage can be derived. However, this approach lacks the capability of acquiring the phase information of the measured signal. As mentioned in [Chapter 1](#), the magnitude and phase of the measured signal are required to determine the bioimpedance. Although, the approach also employs a reference signal that is converted to a PWM signal to provide synchronization. This reference signal is transmitted to the receiver side along with the measured signals. In the proposed design, a similar method can be used in order to additionally obtain phase information of the measured signal. A reference signal can be employed to synchronize the measured signal and the excitation signal. The reference signal can be generated by a resistor with a known value in series with the bioimpedance, similar to [58]. Subsequently, the reference signal is also converted to a PWM signal, as was implemented in [46]. In the following sections, the design and operation of the proposed circuit design will be explained.

In order to demonstrate the efficacy of the proposed system, an excitation source based on a voltage-controlled voltage source is implemented as well, as will be discussed in [Section 3.4.2](#). Furthermore, the PWM-based ATC approach requires a time-to-digital converter (TDC) in order to process the measured information. The proposed system considers the TDC to be on the receiver side rather than part of the transthoracic bioimpedance monitor. First of all, the reason is that this approach reduces complexity of the proposed system and, therefore, saves area. Second, the raw PWM output signals of the proposed system can be used according to the application of a system without the loss of information due to preprocessing. Therefore, a modular system level architecture approach is taken which provides flexibility for the application of the proposed system, as was explained in [Section 2.2](#).

3.1.2. Requirements for Proposed Design

The following set of requirements have been established, according to the information presented in [Chapters 1](#) and [2](#):

- The excitation source should be able of generating a sinusoidal excitation current which amplitude and frequency can be adjusted. Moreover, the excitation source at least complies to the parameter values listed in [Table 2.1](#).

- At least two input channels are required to measure the bioimpedance and the reference signal.
- The proposed system should be able to measure the resistive as well as the capacitive components of the bioimpedance.
- The PWM generator should have a configurable sampling frequency that at least satisfies Nyquist-rate sampling.
- The loss of information should be prevented by avoiding a duty cycle of 0% and 100% of the PWM output signals [63].

3.2. Circuit Design

A circuit diagram of the proposed design of the PWM-based bioimpedance measurement instrumentation is depicted in Fig. 3.1. The following circuit components can be characterized:

- **Excitation Source**

The excitation current I_{exc} is generated by a VCCS, and the driving voltage can be supplied by an voltage generator module or by a local oscillator of the system.

- **Biological Tissue and Reference**

A device under test (DUT) represent the bioimpedance that is to be measured. The DUT can a resistor, a capacitor or a combination of both. The reference is implemented by a resistor R_{ref} with a fixed known value.

- **Bioimpedance Readout and Reference Signal Generator**

These blocks employ an instrumentation amplifier (INA) in each channel in order to amplify and bias the input voltages V_{sig} and V_{ref} into the input range of the PWM generator block.

- **PWM Generator**

The comparators $Comp_{PWM,s}$ and $Comp_{PWM,r}$ generate two PWM output voltages $V_{PWM,s}$ and $V_{PWM,r}$ using a triangular carrier wave.

- **Triangular Wave Generator (TWG)**

The triangular carrier wave V_{tri} is generated by a local oscillator of the system.

The excitation source generates an AC current I_{exc} which is applied to the *DUT* and the reference. Consequently, the voltage V_{sig} can be measured across the *DUT* in response to the excitation current. Furthermore, the voltage V_{ref} across the reference resistor R_{ref} is in-phase with the excitation current and equal to $V_{ref} = I_{exc} \cdot R_{ref}$. Therefore, the magnitude and phase of V_{ref} are known and the voltage can be used as reference. Subsequently, the bioimpedance readout and the reference signal generator both employ an instrumentation amplifier (INA) and signal conditioning. The input voltages V_{sig} and V_{ref} to these blocks are each filtered by a high-pass filter (HPF) to eliminate any DC signal, such as electrode offset and DC currents. Furthermore, the INAs amplify the input voltages into the input range of the PWM generator in order to increase the resolution of the PWM signals, as will be explained in Section 3.3. Lastly, the signals V'_{sig} and V'_{ref} are forwarded to the PWM generator. The PWM generator consist of two comparators for each channel and a triangular wave generator. The output $V_{PWM,s}$ of comparator $Comp_{PWM,s}$ contains the magnitude information of V_{sig} . Similarly, the magnitude information of V_{ref} is modulated in the PWM output $V_{PWM,r}$ of comparator $Comp_{PWM,r}$. Therefore, $V_{PWM,s}$ resembles the measured signal at channel 1 with a phase shift caused by the *DUT* and the PWM signal $V_{PWM,r}$ represents the reference voltage at channel 2 in-phase with excitation current.

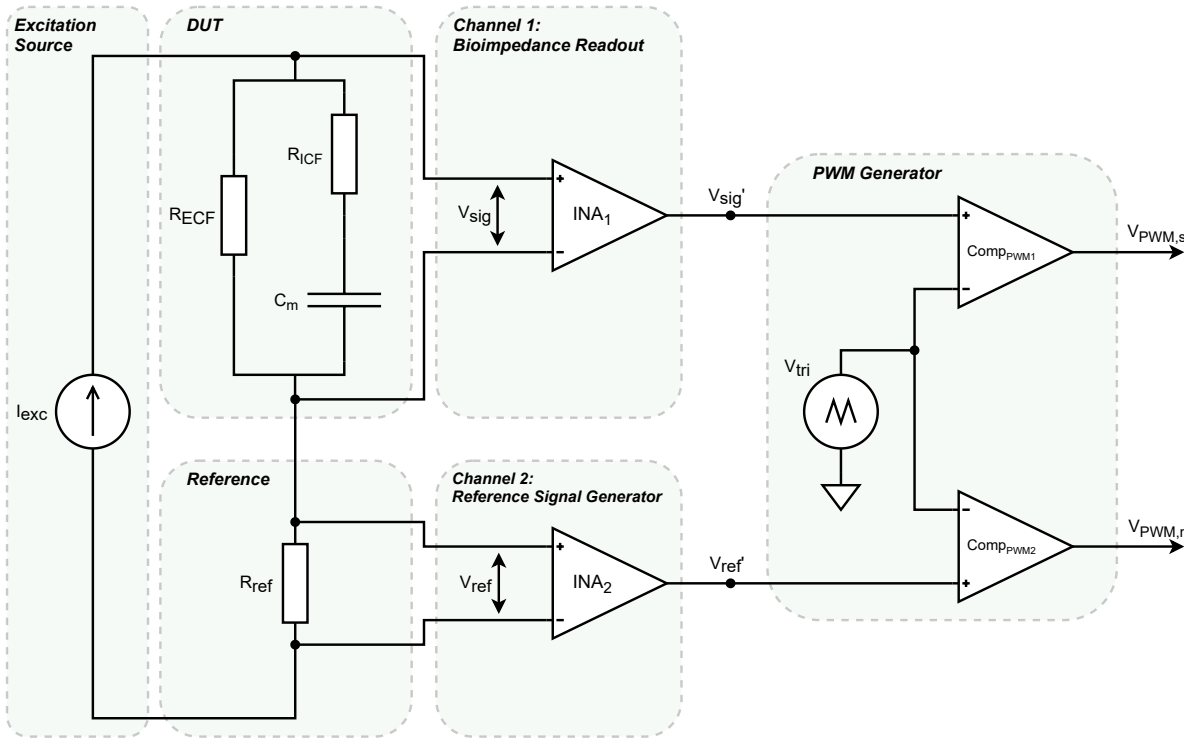


Figure 3.1: Circuit diagram of the proposed PWM-based bioimpedance measurement instrumentation for a wearable bioimpedance monitor. The measured voltage V_{sig} and the reference voltage V_{ref} are converted to PWM signals $V_{PWM,s}$ and $V_{PWM,r}$, respectively.

3.3. PWM Generator

The analog-to-time conversion is employed by the PWM generator. The analog voltages V_{sig} and V_{ref} are modulated into two separate PWM output signals $V_{PWM,s}$ and $V_{PWM,r}$, respectively. Moreover, a TWG is part of the PWM generator and samples the input analog signals in order to produce the PWM signals at the output. This approach in generating PWM signals is illustrated in Fig. 3.2, where V_{sine} represents an analog signal that is converted to a PWM signal V_{PWM} . A triangular wave is a periodic signal that alternates between ramping up to a higher limit V_{TH} and down to a lower limit V_{TL} . The time periods T_u and T_d represents the time that $V_{tri}(t)$ ramps up and down, respectively. Furthermore, the amplitude is given by $|V_{tri}| = \frac{1}{2}(V_{TH} - V_{TL})$. The period of the triangular wave is given by $T_{tw} = T_u + T_d$, and, therefore, the frequency of the triangular wave is $f_{tw} = 1/T_{tw}$. In case of a triangular wave the time periods T_u and T_d are equal. Alternatively, if $T_u \neq T_d$ the waveform is a sawtooth wave.

The PWM output signals represent the voltage levels of V_{sine} by means of a variable duty cycle δ . The duty cycle δ is defined as the ratio between the ON-time or OFF-time, and the period of the PWM signal, as illustrated in Fig. 3.2. The ON-time is defined as the time that the PWM signal is equal to positive supply V_{s+} . Conversely, the time that the PWM signal is equal to the negative supply V_{s-} is named the OFF-time. The period of the PWM signals is equal to the period T_{tw} of the triangular wave. Therefore, the δ is given by:

$$\delta = \frac{T_{on}}{T_{tw}} = 1 - \frac{T_{off}}{T_{tw}} \quad (\times 100\%) \quad (3.1)$$

Since the ON-time and OFF-time vary depending on the voltage level of V_{sine} , the average of V_{PWM} changes as well. The average value \bar{V}_{PWM} in one period T_{tw} is given by:

$$\bar{V}_{PWM} = \delta \cdot V^+ + (1 - \delta) \cdot V^- \quad (3.2)$$

Ideally, the voltage levels at the input of the PWM generator can range from V_{s-} to V_{s+} . Therefore, in order to ensure efficacy of the PWM generator $V_{s-} \leq V_{TL}$ and $V_{s+} \geq V_{TH}$. A duty cycle of $\delta = 0\%$ is therefore equal to an input voltage of V_{s-} . Conversely, a input voltage of V_{s+} is represented by $\delta = 100\%$. However, setting the input range equal to the supply could deteriorate the efficacy of PWM generator

which results in the loss of information. Therefore, a margin on the input voltage range from the supply levels ensures preservation of the voltage information at the cost of a smaller input voltage range of the PWM generator. This precaution translates to δ never being 0% or 100%, and the voltage range of V_{tri} should be greater than the input voltage range.

The resolution of the PWM signal is set by the input voltages range of PWM generator, and the upper and lower limits of V_{tri} . Namely, setting the limits of V_{tri} slightly above the input voltage range maximizes the resolution of the PWM generator. In practice, the limits of V_{tri} are fixed and the resolution of $V_{PWM,s}$ varies with the DUT . However, the reference resistor R_{ref} can be chosen and fixed in such a way that the range of V_{ref} very close to the limits of V_{tri} . Therefore, increasing the resolution for $V_{PWM,r}$ would increase the accuracy of the system regarding the determination of the phase shift caused by the DUT . Another method to improve the accuracy of the system is to increase the sampling frequency. First of all, this approach reduces the error introduced by natural sampling. By increasing the sampling frequency, the two level crossings in one period move closer to the same voltage level and therefore increasing the accuracy of the PWM generator. Secondly, increasing the sampling frequency also increases the pulses generated by the PWM generator. Therefore, increasing the sampling frequency proportionally increases the accuracy of the system.

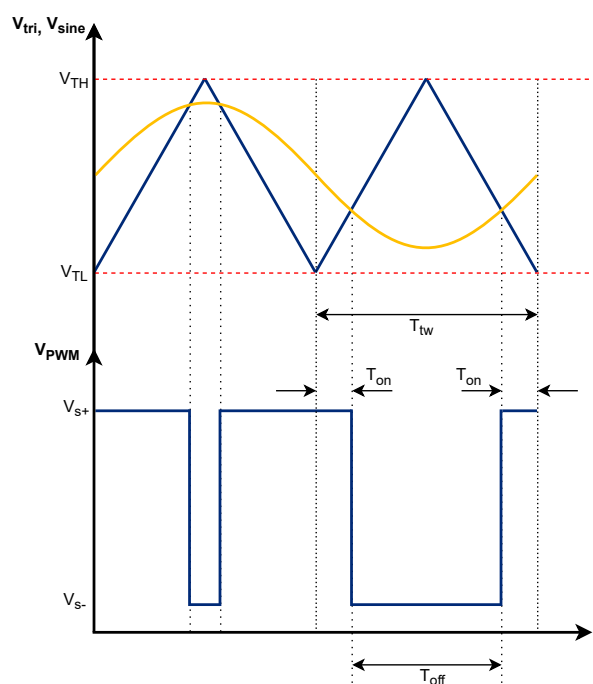


Figure 3.2: Signals of the PWM generator. The input signals to the comparators $Comp_{PWM,s}$ and $Comp_{PWM,r}$ are sinusoidal signals represented by V_{sine} and the triangular wave signal V_{tri} . The PWM output signal of the comparators are illustrated by V_{PWM} .

3.3.1. Triangular Wave Generator Design

In the proposed system design, a practical triangular wave generator (TWG) is designed and implemented as a local oscillator in the measurement instrumentation. The operation of the TWG can be described by an first-order oscillator, depicted in Fig. 3.3. A oscillator is capable of producing a periodic signal out of a constant, and needs to perform four function: *integration*, *comparison*, *switching the sign of the integration constant*, and *memorization* [65]. First of all, a time-variant signal $E_0(t)$ is produced from a integration constant α by an integrator. Consequently, to prevent $E_0(t)$ to grow out of bounds, α should be changed. The most convenient way is to inverse the sign of α . In order to determine when to inverse the sign of α , $E_0(t)$ should be compared with constant reference levels. In case $E_0(t)$ reaches the high reference level E_h , the sign of α becomes negative. Conversely, when $E_0(t)$ reaches the low reference level E_l , the sign of α becomes positive. Lastly, the polarity of the sign needs to be stored in a memory, and changed. Only two states of α needs to be stored, therefore, a binary memory will suffice. In Fig. 3.3a, a block diagram of the above described first-order oscillator is shown. Each function of the

oscillator is represented by a separate block. A simplified block diagram is depicted in Fig. 3.3b, where the Schmitt trigger integrate three functions in one block. Although, the simplicity of this configuration comes at the cost of the easy to optimize each separate function.

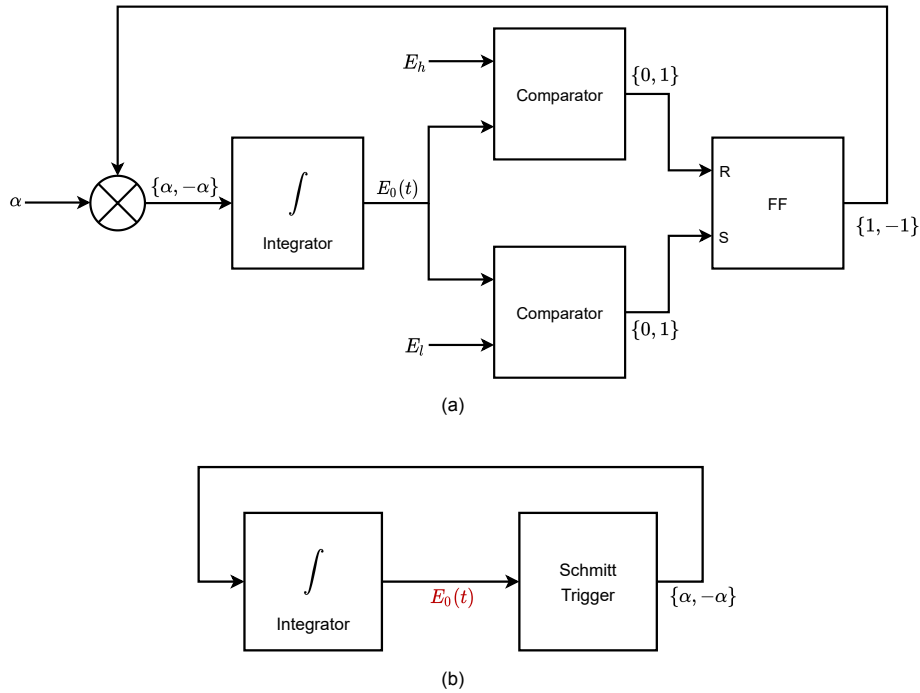


Figure 3.3: Block diagram of a first-order oscillator. (a) A basic first-order oscillator with each of the function represented by separate blocks. (b) A simplified representation with three of the functions, except for integration, combined in the Schmitt Trigger. Figure adapted from [65].

Practical implementations of a first-order oscillator conventionally implement the integrator by an capacitor C_{int} . Therefore, the output of the integrator is a voltage, and the integration constant is proportional to a constant current and, moreover, equal to $\alpha = I_{int}/C_{int}$. The periodic integrator output E_0 is a triangular wave characterized by the charging and discharging of C_{int} . The voltage E_0 can be illustrated similarly by V_{tri} in Fig. 3.2. Therefore, the bound of E_0 are given by $E_h = V_{TH}$ and $E_l = V_{TL}$. The integration constant α is represented by the slope of V_{tri} , and, lastly, T_{tw} is the period of V_{tri} .

In the proposed system, the circuit implementation of the TWG follows the Schmitt trigger approach of a first-order oscillator presented in Fig. 3.3b. The reason for the implementation of this approach is that the Schmitt trigger can be implemented by a single comparator with added hysteresis, as depicted in the circuit diagram of the oscillator design in Fig. 3.4. The waveform diagram of the oscillator circuit is illustrated in Fig. 3.5. As a result of the Schmitt trigger approach, the number of required components is reduced compared to the approach of Fig. 3.3a. Hysteresis is provided by the resistors R_{st1} and R_{st2} by means of positive feedback. Therefore, when V_{tri} exceeds one of the two reference levels the output $V_{out,st}$ is forced to the positive V_{s+} or negative V_{s-} supply. The reference levels V_{TH} and V_{TL} , illustrated in Fig. 3.5a, and are defined as $V_{TH} = -V_{s-} \cdot (R_{st1}/R_{st2})$ and $V_{TL} = -V_{s+} \cdot (R_{st1}/R_{st2})$. Assuming that V_{tri} will be a periodic triangular wave signal, the output $V_{out,st}$ is a square wave that alternates between V_{s+} and V_{s-} . Moreover, the time periods shown are determined by the periodic triangular wave input as well. As mentioned previously, the Schmitt trigger implement three functions of a first-order oscillator. However, the implementation in Fig. 3.3b yet provides the possibility to optimize certain functions separately according to its application, such as the reference levels or the oscillation frequency.

Conventionally, the constant current required at the input of the integrator is implemented by an resistor. Therefore, the integrator block can be represented by the integrator circuit depicted in Fig. 3.4. The input square wave signal generates a constant current $I_{int} = V_{out,st}/R_{int}$. Subsequently, the capacitor C_{int} is charged or discharged by I_{int} depending on the voltage at $V_{out,st}$. As a result, the output voltage $V_{tri} = \int -I_{int}/C_{int} dt$, as illustrated in Fig. 3.5b. During time duration T_u , the integrator input $V_{out,st} = V_{s-}$ and the slope of V_{tri} is $s_1 = -V_{s-}/(R_{int} \cdot C_{int})$, and C_{int} is charged. Subsequently,

C_{int} is discharged during time duration T_d , where $V_{out,st} = V_{s+}$ and slope $s_2 = -V_{s+}/(R_{int} \cdot C_{int})$. As a result of V_{tri} being periodic, the period $T_{tw} = T_u + T_d$ where $T_u = T_d$ and the slopes $s_1 = -s_2$. Therefore, the amplitude $|V_{tri}|$ and the frequency f_{tw} of the V_{tri} are given by:

$$|V_{tri}| = |V_{out,st}| \frac{R_1}{R_2} \quad (3.3)$$

$$f_{tw} = \frac{1}{T_{tw}} = \frac{R_2}{4R_1 R_{int} C_{int}} \quad (3.4)$$

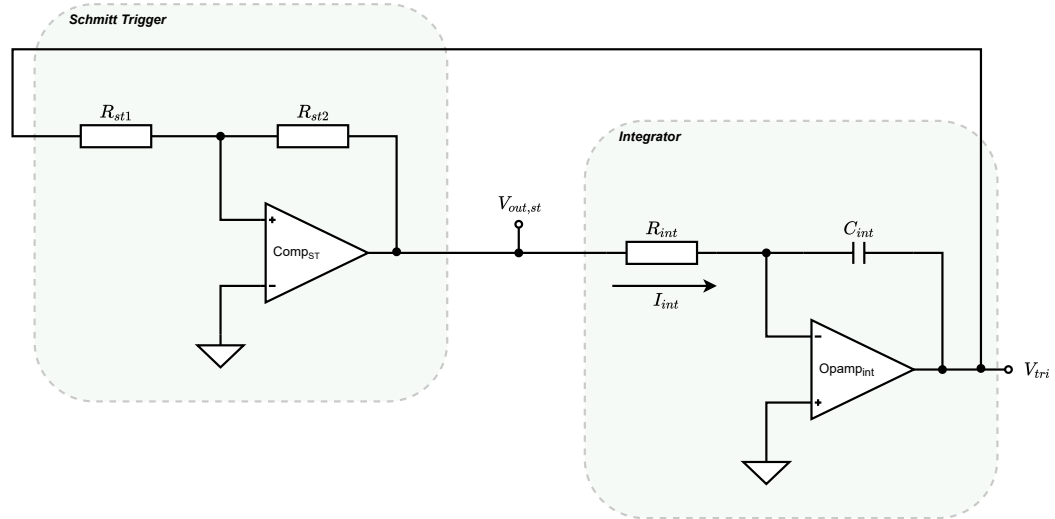


Figure 3.4: Local oscillator design of the implemented triangular wave generator. The Schmitt trigger circuit produces a square wave signal at the output $V_{out,st}$. The square wave is then integrated into a triangular wave V_{tri} and fed back to the Schmitt trigger.

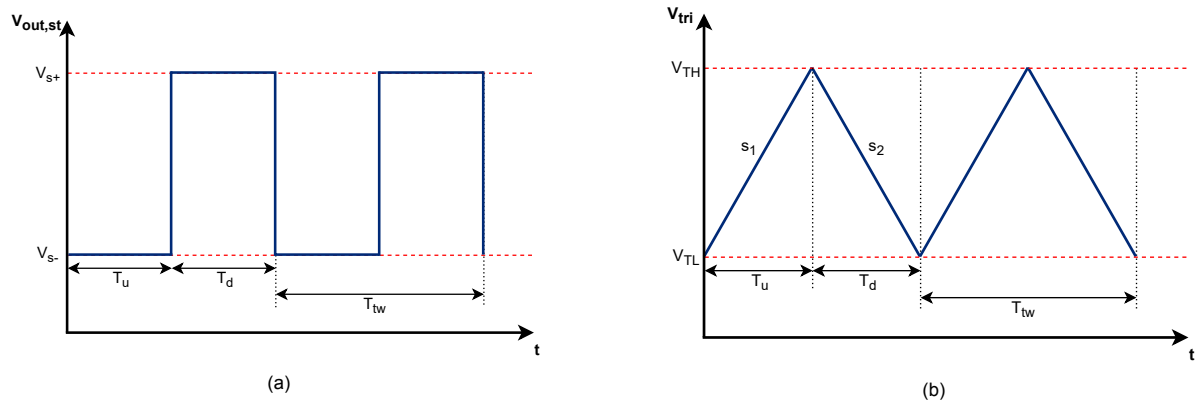


Figure 3.5: Timing diagram of the triangular wave generator. (a) The output voltage $V_{out,st}$ of the Schmitt trigger. (b) The output triangular wave signal V_{tri} of the integrator circuit.

3.3.2. Non-ideal Circuit Operation

The employment of real components in the system introduces inaccuracies to the measured signals. Therefore, these sources of inaccuracy should be determined and, accordingly, the effect on the system performance analyzed.

First of all, the INAs introduces a delay at the output. Moreover, increasing the gain of the INAs results in a decreasing bandwidth and, therefore, a larger phase shift is produced at the output. In order to minimize the effect of the phase error, the gain of the INAs in both channels should be set equally. Subsequently, this error can be characterized and eliminated by calibration.

Secondly, the comparators $Comp_{PWM,s}$ and $Comp_{PWM,r}$ have a propagation delay that affects the PWM outputs. Although, when the propagation delay is kept much smaller than the period of the triangular wave the effect is minimized. Furthermore, the two channels are set up identically which reduces any delay error introduced by the comparators.

Lastly, the TWG also employs a comparator that has a propagation delay as previously described. The same measures apply to this comparator as well. Moreover, the operational amplifier (opamp) that implements the integrator in the TWG has a limited slew rate and bandwidth which can affect the performance of the TWG. The slew rate of the opamp should at least be greater than $4 \cdot |V_{tri}| \cdot f_{tw}$ in order to ensure linearity of the triangular wave. Furthermore, the triangular wave with a fundamental frequency of f_{tw} is an infinite summation of sinusoids at the odd harmonic. Therefore, the gain-bandwidth of the opamp should accommodate harmonics at least until the 10th harmonic in order to prevent distortion of the triangular wave [61].

3.4. PCB Prototype

The proposed system design is validation by a PCB prototype. The circuit diagram of the implemented PCB is depicted in Fig. 3.6. The figure is derived from Fig. 3.1 with additional components to ensure the efficacy of the implemented circuit. In the following section the operation of the implemented PCB will be discussed. The voltage V_{sig} across the DUT at channel 1 is measured by inputs In_1 and In_2 . Furthermore, the inputs In_3 and In_4 of channel 2 measure the voltage V_{ref} across the reference resistor R_{ref} . As can be observed from Fig. 3.1, inputs In_2 and In_3 will commonly be connected together. The output channels Out_1 and Out_2 are equivalent to the PWM outputs $V_{PWM,s}$ and $V_{PWM,r}$, respectively. The excitation current is applied to the DUT and R_{ref} , as depicted in Fig. 3.1. The excitation circuit is implemented by an voltage-controlled current source, which will be explained in Section 3.4.2.

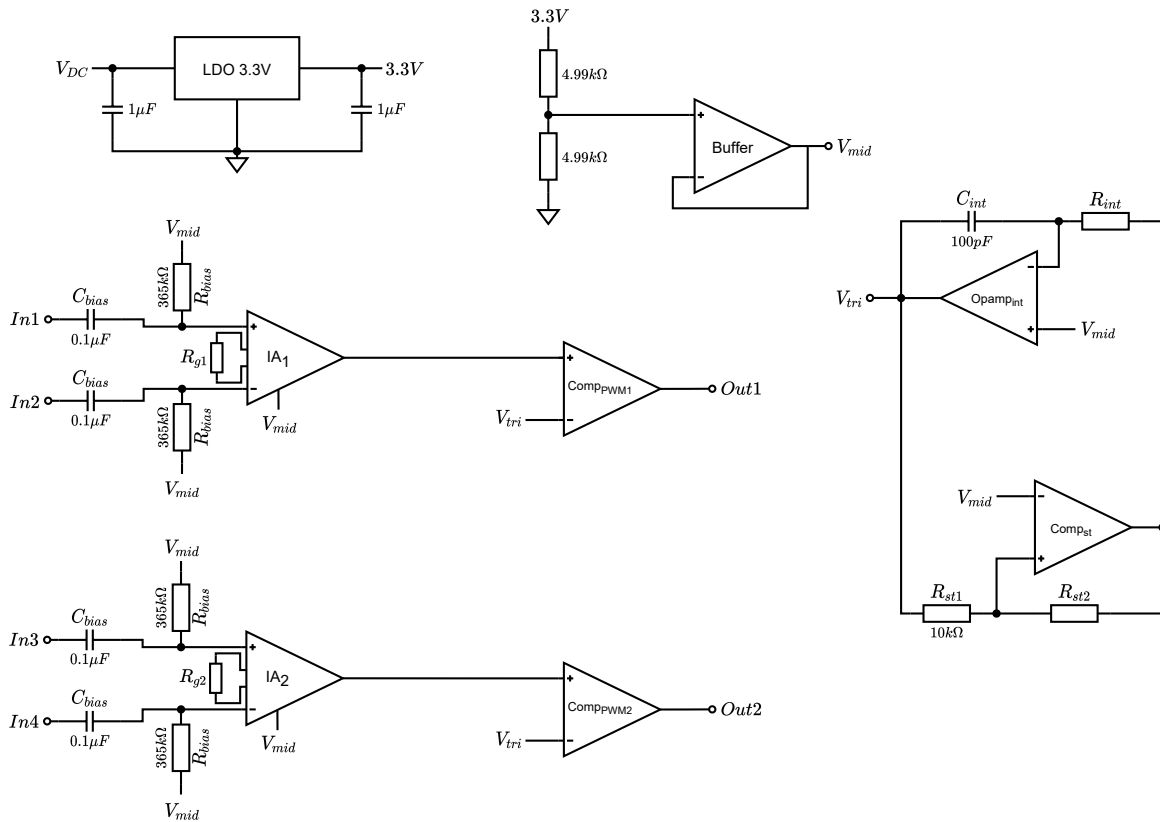


Figure 3.6: Circuit diagram of the implemented PCB.

3.4.1. PCB Implementation

The PCB is provided with power at V_{DC} from an external single supply. A low-dropout (LDO) regulator on the PCB is used to generate a stable 3.3 V which, subsequently, is employed to power the entire PCB and all the associated integrated circuits (ICs). Therefore, the previously mentioned supply voltage are equal to $V_{s+} = 3.3V$ and $V_{s-} = 0V$. The LDO regulator from *Microchip Technology* that is used requires only a dropout voltage of 350 mV when fully loaded. Therefore, the power consumption for generating a 3.3 V supply for the overall PCB can be kept low compared to other types of voltage regulators. Additionally, a mid-supply reference voltage V_{mid} of 1.65 V is generated from a voltage divider followed by a buffer. The voltage reference V_{mid} is employed in order to bias several signals above 0 V and, therefore, no additional negative supply is required to the PCB.

In [Section 3.3.1](#) the design of the TWG was discussed, and the frequency and amplitude of the triangular wave V_{tri} are essential design parameters. First of all, the integrator and the comparator of the TWG are biased at V_{mid} . Therefore, raising all the associated signals above 0 V. Secondly, the upper V_{TH} and lower V_{TL} limit of triangular wave are set to $V_{s+} - 0.1V$ and $V_{s-} + 0.1V$, respectively. Therefore, a wide swing range of V_{tri} of $3.1V_{pp}$ is provide while ensuring the supply rails are not exceeded. Furthermore, the frequency f_{tw} of the triangular wave is chosen to be 400 kHz based on [\[46\]](#). Moreover, potentiometers are employed for R_{st1} and R_{int} to adjust the frequency and analyze the effect on the performance of the system. A comparator of *Texas Instruments* is chosen with a propagation delay $t_{pd} = 4.5\text{ ns}$ for all the comparators on the PCB. For $T_{tw} \gg t_{pd}$ ensures the efficacy of the circuit. Lastly, an opamp from also *Texas Instruments* is implemented in the TWG. The slew rate of the opamp is $25\text{ V}/\mu\text{s} \gg 4 \cdot 1.55\text{ V} \cdot 400\text{ kHz} = 2.48\text{ V}/\mu\text{s}$ and, therefore, linearity of the triangular wave is ensured. Furthermore, the GBW of the opamp is 50 MHz which is enough to accommodate until the 10th harmonics with a fundamental frequency equal to 400 kHz.

The signal path of both input channels are identical to reduce any mismatch between the inputs. To begin with, high-pass filtering and biasing are provided by C_{bias} and R_{bias} . The HPF rejects the any DC signals and the voltage V_{mid} connected to the resistors ensure that the input signals are raised above the negative supply. The output of the IAs is biased by V_{mid} as well. Furthermore, the gain of the INAs are determined by the resistor R_g . As mentioned before, by setting the gain of both the INAs equally the error between the channels is minimized. A instrumentation amplifier of *Analog Devices* has been implemented for the INAs. Subsequently the gain is configured to $12.27\text{ V}/\text{V}$ by fixing $R_{g1} = R_{g2} = 11\text{ k}\Omega$. Therefore, setting a maximum magnitude range of the *DUT* to approximately $1\text{ k}\Omega$ which complies with the typical values of [Table 2.2](#).

The input range to the PWM generator is determined by the constraints on the PWM output signals and, therefore, also setting the maximum range of the *DUT* mentioned before. A duty cycle range of 10% – 90% is chosen to guarantee the efficacy of the PWM generator. Therefore, the input range of the PWM generator is $0.33\text{ V} - 2.97\text{ V}$.

3.4.2. Excitation Circuit Implementation

A voltage-controlled current source is designed in order to implement the excitation current to the system, according to the parameters specified in [Table 2.1](#). First of all, a dual supply of $\pm 5\text{ V}$ powers the opamp in order to facilitate differential signals. Secondly, the VCCS circuit is connected externally to the PCB prototype and the circuit diagram is depicted in [Fig. 3.7](#). The signal generator $V_{exc,in}$ delivers an AC voltage to the circuit, and sets the amplitude and frequency of the excitation current I_{exc} . Input resistor R_{exc} has a fixed value of $10\text{ k}\Omega$ and, consequently, sets the input voltage range of $V_{exc,in}$ to $0.01\text{ V}_{pp} - 1\text{ V}_{pp}$ in order to implement an excitation current between $1\text{ }\mu\text{A} - 100\text{ }\mu\text{A}$. Furthermore, the load comprise the bioimpedance and the reference resistor connected in series, and R_{exc} determines the range of the load well within the limits established in [Table 2.2](#). In [Fig. 3.8](#) the PCB prototype is shown and the associated list of components is specified in [Table 3.1](#).

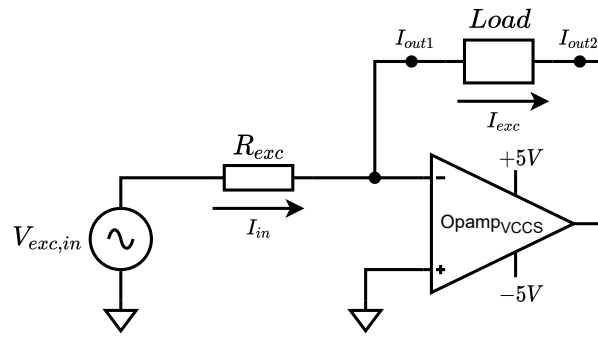


Figure 3.7: Circuit diagram of the implemented excitation current source.

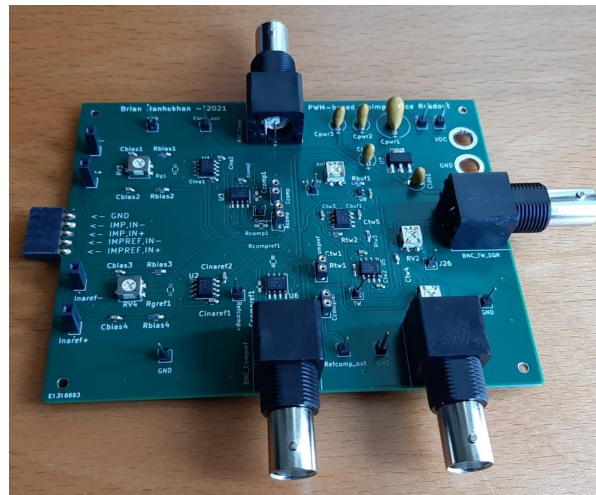


Figure 3.8: The prototype PCB

Table 3.1: List of selected components for PCB implementation.

Function	Selected Component
LDO 3.3V	TC1262-33 CMOS Low-dropout Regulator
Buffer	LMV831 Operational Amplifier
Comp _{st} , Comp _{PWM,s} , Comp _{PWM,r}	TLV3501 High-Speed Comparator
Opamp _{int}	OPA365 Operational Amplifier
INA ₁ , INA ₂	AD8227 Instrumentation Amplifier
Opamp _{VCCS}	A822 Operational Amplifier

4

Results

The designed system is validated by means of two methods. First, simulations are executed employing the designed circuit using the circuit simulation program LTspice[®]. Second, the PCB prototype is tested and the behavior of employing real components in the designed system is evaluated.

4.1. System Simulations

The spice models of the components in Table 3.1 are implemented in LTspice[®] and the proposed circuits presented in Figs. 3.6 and 3.7 are simulated. The *DUT* is connected to channel 1 and the reference resistor R_{ref} is connected to channel 2. Additionally, the outputs I_{out1} and I_{out2} of the excitation circuit are connected to the inputs In_1 and In_4 of the proposed system, respectively.

Firstly, the correct operation of the circuit is validated and, therefore, it is set up in the following manner. An excitation current I_{exc} with an amplitude of 100 μ A and a frequency of 10 kHz is employed. Furthermore, the frequency of the triangular wave V_{tri} is set to 400 kHz. The *DUT* is equal to 1 k Ω and purely resistive, and the $R_{ref} = 500 \Omega$ in order to demonstrate two distinct PWM signals at the output. Also, $R_{g1} = R_{g2} = 11 \text{ k}\Omega$ which sets the gain of the INAs to 12.27 V/V. The resulting signals in one period of I_{exc} are presented in Fig. 4.1. It can be observed that an excitation current of 100 μ A is implemented and the output signals $V_{sig'}$ and $V_{ref'}$ of the INAs stay within the bounds of the triangular wave. Furthermore, the duty cycle range of $V_{PWM,s}$ is greater than the duty cycle range of $V_{PWM,r}$. The described characteristic is to be expected since the amplitude of $V_{sig'}$ is greater than the amplitude of $V_{ref'}$. Despite the efficacy of the proposed, a time delay at the output of the INAs can be observed compared to the excitation current, as depicted in Fig. 4.2. The time delay is identical for both the output signals and equal to 1.32 μ s. As explained in Section 3.3.2, the limited performance of the INAs introduces the time delay at their output. However, the gain of the INAs are set equally and the rest of the input channel are also implemented identical. Therefore, the mismatch between the channel is minimized, resulting in a equal time delay which can be eliminated by calibration.

4.2. System Accuracy

Next, the accuracy of the system is evaluated by means of simulations in LTspice[®] and by measurements on the PCB. The assessment is performed under the same conditions as the previous set-up. However, R_{ref} is set to 1 k Ω so that the resolution of the $V_{PWM,r}$ is increased. In order to evaluate the accuracy of the system, the magnitude and phase are derived from the output PWM signals and compared with the actual *DUT*, with the use of the numerical computing program Matlab[®]. Considering deriving the magnitude, the duty cycle of $V_{PWM,s}$ is determined per sampling period T_{tw} . Subsequently, the minimum and maximum duty cycle is used to derive the peak-to-peak voltage of the measured $V_{sig'}$. Finally, since the gain of the INA and the amplitude of I_{exc} are known, the magnitude of the measured *DUT* can be determined. Regarding the phase shift of the *DUT*, the 50% duty cycle crossings of both $V_{PWM,s}$ and $V_{PWM,r}$ are used. The time difference between these two time instances form the time delay between the signals. Subsequently, the phase shift can be derived and a negative phase shift indicated that $V_{PWM,s}$ lags behind $V_{PWM,r}$. To begin with, a purely resistive *DUT* is varied and, subsequently, the

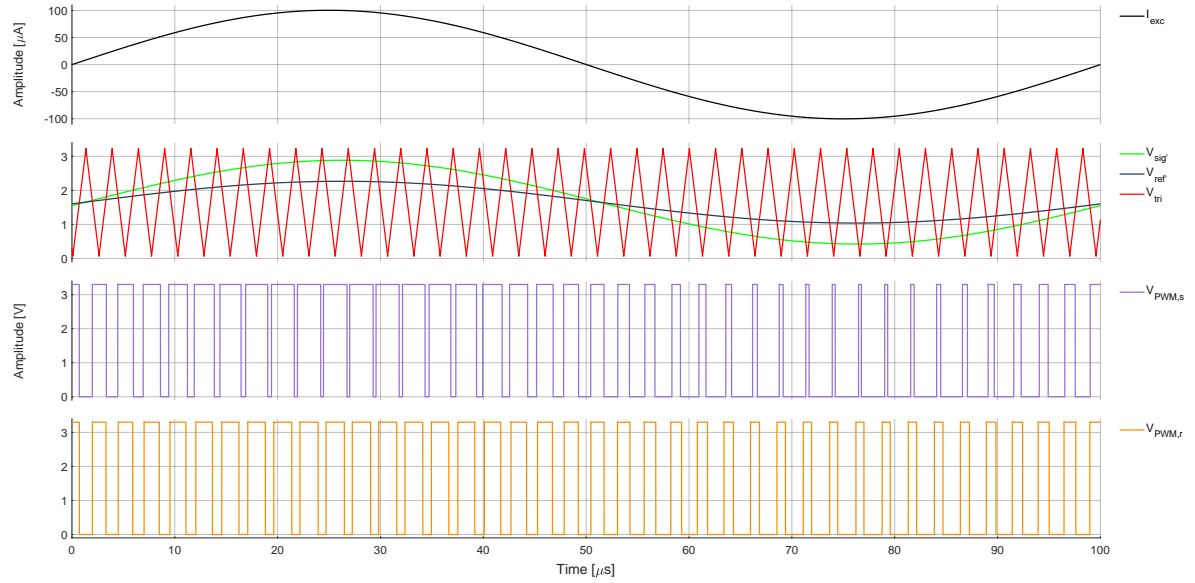


Figure 4.1: LTspice[®] simulation: the resulting signals in a single period $t_{exc} = 100 \mu\text{s}$ of the excitation current I_{exc} are shown. The load consist of a $DUT = 1 \text{ k}\Omega$ and $R_{ref} = 500 \Omega$.

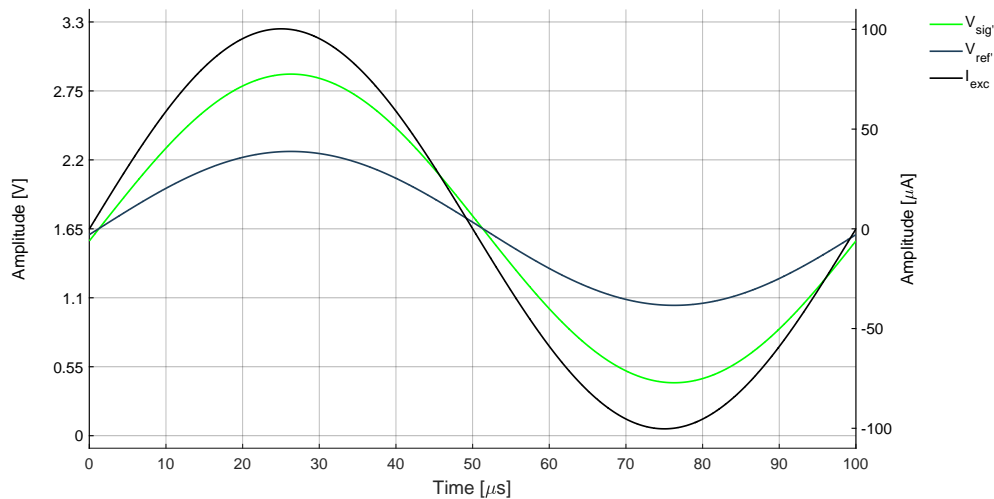


Figure 4.2: LTspice[®] simulation: the output $V_{sig'}$ and $V_{ref'}$ of the INAs present a time delay of approximately $1.33 \mu\text{s}$ in comparison to the excitation current I_{exc} .

magnitude and phase are extracted from the PWM signals. Afterwards, the same tests are performed on a purely capacitive DUT and, lastly, on a DUT consisting of a RC -combination. This procedure is followed as a result of the electrical bioimpedance model presented in Fig. 1.1, where the model consist of resistive and capacitive elements.

4.2.1. Resistive DUT

The figures Figs. 4.3 and 4.4 show the validation results of the magnitude and phase, respectively, of a purely resistive DUT which is varied between $0 \Omega - 1 \text{ k}\Omega$. It is to be expected that the magnitude of the DUT is equal to the resistor value and the phase shift caused by the DUT is zero. In Fig. 4.3, the results regarding the magnitude of the DUT are depicted. The magnitude of $V_{PWM,s}$ is compared with the actual magnitude of the DUT . Furthermore, the amplitude of $V_{sig'}$ is considered as well in order to characterize the errors before $V_{PWM,s}$ is generated. The measured $V_{PWM,s}(meas)$ and $V_{PWM,r}(meas)$ at the output of the PCB are performed by taking $N = 10$ samples for each measured DUT . In A of

Fig. 4.3, the absolute magnitudes of the evaluated signals are depicted, where the black line indicates the actual magnitude of the *DUT*. Subsequently, in B of Fig. 4.3 the absolute magnitude error between the evaluated signals and the actual *DUT* is displayed. Lastly, the relative magnitude error between the evaluated signals and the actual *DUT* can be observed in C of Fig. 4.3. From the fitting curves in B it can be observed that $V_{P_{W_{M,s}}}(meas)$ show a large offset error compared to the simulated results. This observation can be explained by the additional noise introduced in the PCB implementation. The offset of $V_{P_{W_{M,s}}}(meas)$ is equal to $30.33\ \Omega$ and indicates the error causes by the noise floor being reached. This produces the increasing relative errors for lower magnitude values of the *DUT*. Furthermore, the slopes of $V_{P_{W_{M,s}}}$ and $V_{P_{W_{M,s}}}(meas)$ are $61\ \text{m}\Omega/\Omega$ and $76\ \text{m}\Omega/\Omega$, respectively, and represent the gain error. Although, the difference between this slopes is small. Therefore, calibrating the system for the offset decreases the error between the simulated and measured results. Also, the slope of $V_{sig'}$ is $6\ \text{m}\Omega/\Omega$ and a large difference between the other slopes can be observed. This difference can be explained by the accuracy of the PWM generator and it can be reduced, for instance, by increasing the sampling frequency, as explained in Section 3.3.

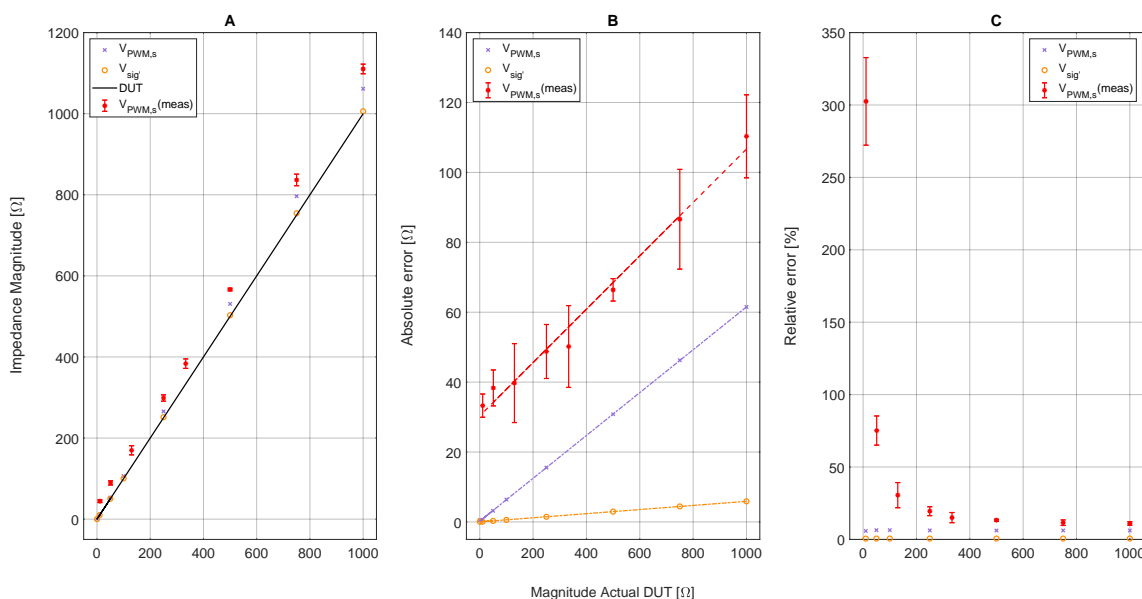


Figure 4.3: Magnitude measurements on a pure resistive *DUT*: (A) the magnitude of $V_{P_{W_{M,s}}}$, $V_{sig'}$ and $V_{P_{W_{M,s}}}(meas)$ are evaluated and compared with the actual magnitude of the *DUT*. (B) The absolute magnitude error of the evaluated signals compared to the *DUT*. (C) The relative magnitude error of the evaluated signals compared to the *DUT*.

The results regarding the phase of the *DUT* are depicted in Fig. 4.4. In A and B of Fig. 4.4, the absolute and relative phase shift of $V_{P_{W_{M,s}}}(meas)$ with respect to the reference PWM output $V_{P_{W_{M,r}}}(meas)$, respectively. These figures show an increase in the phase shift, which is equal to the phase error presented in A of Fig. 4.4, can be observed for lower values of the *DUT*. Similarly to the magnitude results, this can be explained by the decreasing SNR at the input of INA_s . This results in time jitter, as explained in Section 3.3.2.

4.2.2. Capacitive DUT

Next, a purely capacitive *DUT* is evaluated and R_{ref} is kept as a pure resistor. The capacitor values are chosen so the magnitude range of the *DUT* is $0\ \Omega - 1\ \text{k}\Omega$ in order to avoid saturation of INA_1 . The expectation is that the magnitude will show comparable behavior as was observed for the purely resistive *DUT*. Contrarily, the phase shift is expected to be equal to -90° . In Fig. 4.5, the magnitude derived from $V_{P_{W_{M,s}}}(meas)$ is compared with the magnitude of the actual *DUT*, where the latter is depicted by the black line. The linear curve shown in B of Fig. 4.5 fits approximately all the data points of $V_{P_{W_{M,s}}}(meas)$ and the offset equal to $21.35\ \Omega$. Furthermore, the slope of the curve is $94\ \text{m}\Omega/\Omega$. Similar to the magnitude of the resistive *DUT*, it can be observed that the relative magnitude error in C of Fig. 4.5 increases with decreasing magnitude values of the *DUT* due to noise.

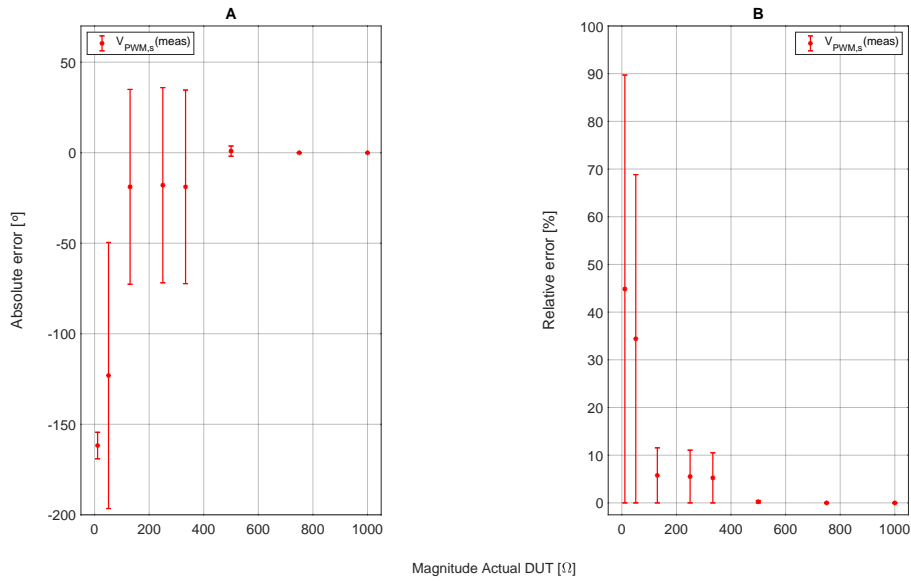


Figure 4.4: Phase measurements on a pure resistive *DUT*: (A) The absolute phase shift of $V_{PWM,s}(meas)$ is evaluated with respect to $V_{PWM,r}(meas)$. (B) The relative phase shift of $V_{PWM,s}(meas)$ is evaluated with respect to $V_{PWM,r}(meas)$.

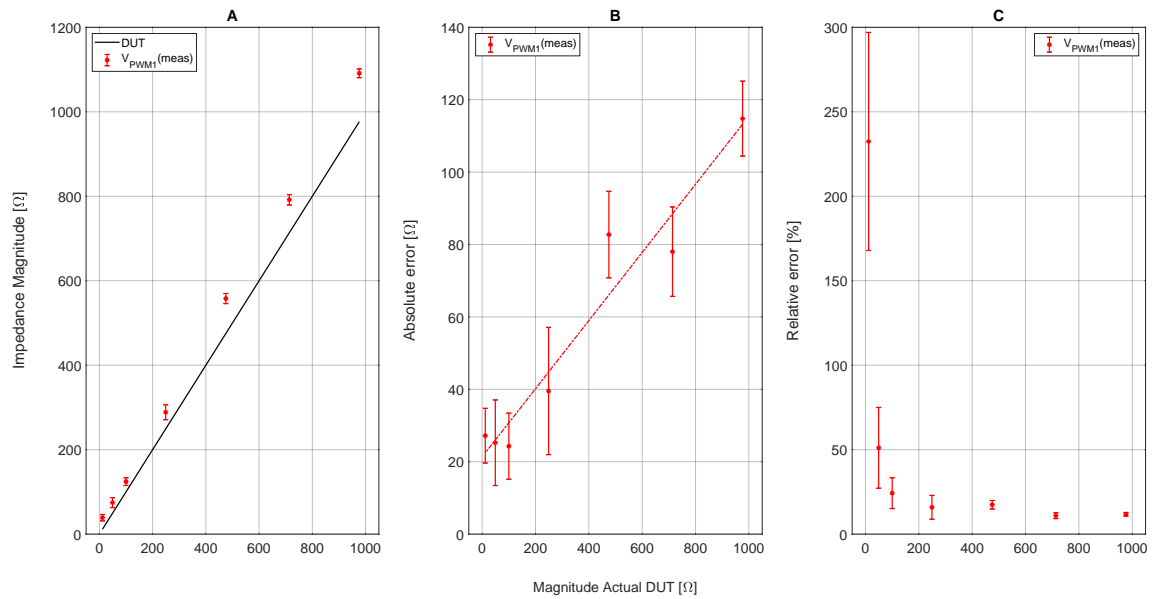


Figure 4.5: Magnitude measurements on a pure capacitive *DUT*: (A) the magnitude of $V_{PWM,s}(meas)$ is evaluated and compared with the actual magnitude of the *DUT*. (B) The absolute magnitude error of $V_{PWM,s}(meas)$ compared to the *DUT*. (C) The relative magnitude error of $V_{PWM,s}(meas)$ compared to the *DUT*.

In Fig. 4.6, the phase shift of $V_{PWM,s}(meas)$ is evaluated with respect to $V_{PWM,r}(meas)$ and the relative error compared to the expected -90° phase shift. In A of Fig. 4.6, a phase shift of approximately -90° can be observed for higher *DUT* magnitudes. For lower magnitude values of the *DUT* the relative error, as illustrated in B of Fig. 4.6, increases due to time jitter.

4.2.3. Resistive and Capacitive DUT

Lastly, a *DUT* consisting of a parallel combination of a resistor and a capacitor (RC-combination). A upper limit for the *DUT* magnitude of 1 kΩ is still uphold in order to prevent INA_1 from saturating. The following RC-combinations are used: 1 kΩ || 1 nF, 750 Ω || 1 nF, 500 Ω || 1 nF and 250 Ω || 10 nF. In Figs. 4.7 and 4.8, the magnitude and the phase shift as a result of the *DUT* are evaluated, respectively.

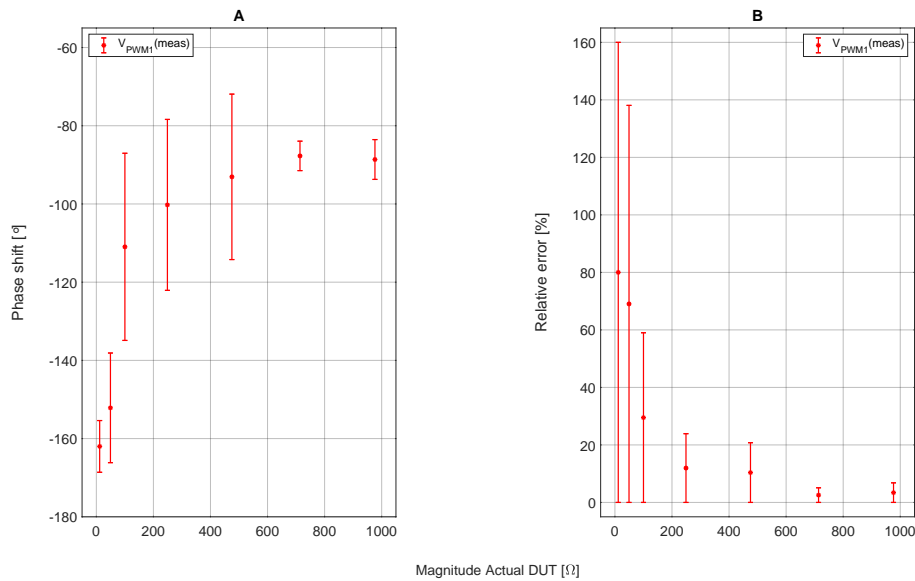


Figure 4.6: Phase measurements on a pure capacitive DUT: (A) The phase shift of $V_{P_{PWM_1}(meas)}$ is evaluated with respect to $V_{P_{PWM_1}(meas)}$. (B) The relative phase error of $V_{P_{PWM_1}(meas)}$ is evaluated with respect to the expected phase shift of -90° .

Moreover, the expected values for the magnitude and phase shift are depicted in both the figures, where it is to be expected that the magnitude of the DUT follows the black line in A of Fig. 4.7. Furthermore, the black crossed markers in A of Fig. 4.8 indicates the calculated phase of the DUT. Also, $V_{P_{PWM_1}(meas)}$ is identical to $V_{P_{PWM_1}(meas)}$ in the previous measurements. Regarding the magnitude of the DUT, a similar behavior can be observed as was seen for the purely resistive and purely capacitive measurements. The relative error increases with a decreasing DUT magnitude. However, the absolute error in B of Fig. 4.7 do not fit on a linear fitting curve which makes calibration more difficult, as explained in Section 3.3.2.

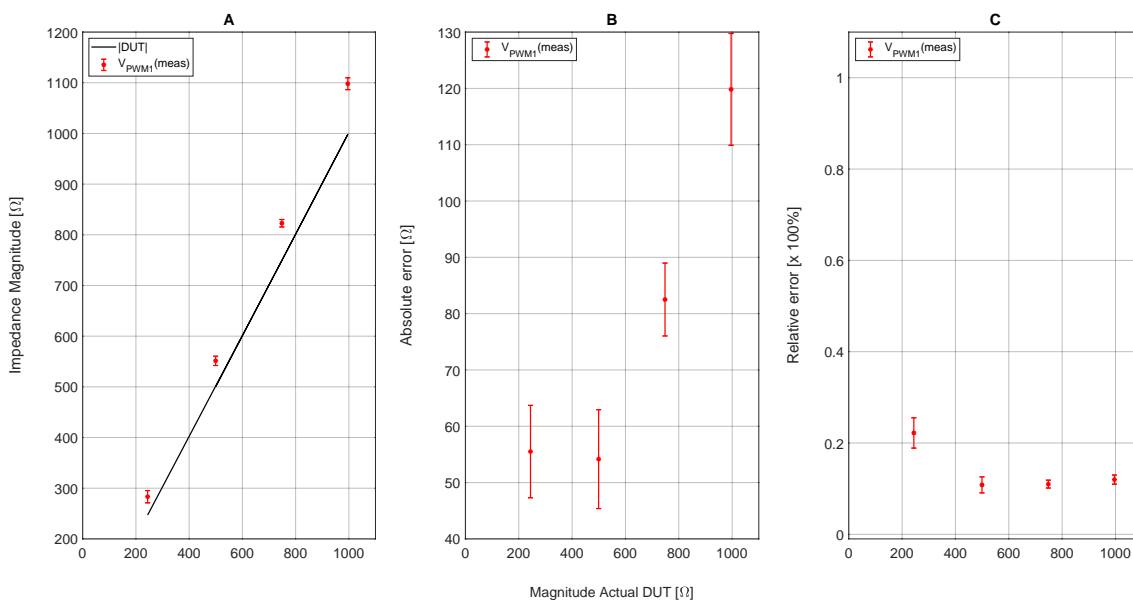


Figure 4.7: Magnitude measurements on a RC parallel combination as DUT: (A) the magnitude of $V_{P_{PWM_1}(meas)}$ is evaluated and compared with the actual magnitude of the DUT. (B) The absolute magnitude error of $V_{P_{PWM_1}(meas)}$ compared to the DUT. (C) The relative magnitude error of $V_{P_{PWM_1}(meas)}$ compared to the DUT.

In A of Fig. 4.8, $V_{P_{PWM1}}(meas)$ indicates the phase shift of $V_{P_{PWM1}}(meas)$ with respect to $V_{P_{PWM,r}}(meas)$. Furthermore, the absolute phase error with the expected phase shift, indicated by the black crossed markers, can be observed. The relative error of the measured phase shift with respect to the calculated phase shift is depicted in B of Fig. 4.8. The phase measurements show a relatively low error, except for the $250 \Omega \parallel 10 \text{ nF}$ as the *DUT*, which was expected from the previous measurement with a purely resistive *DUT* and purely capacitive *DUT*.

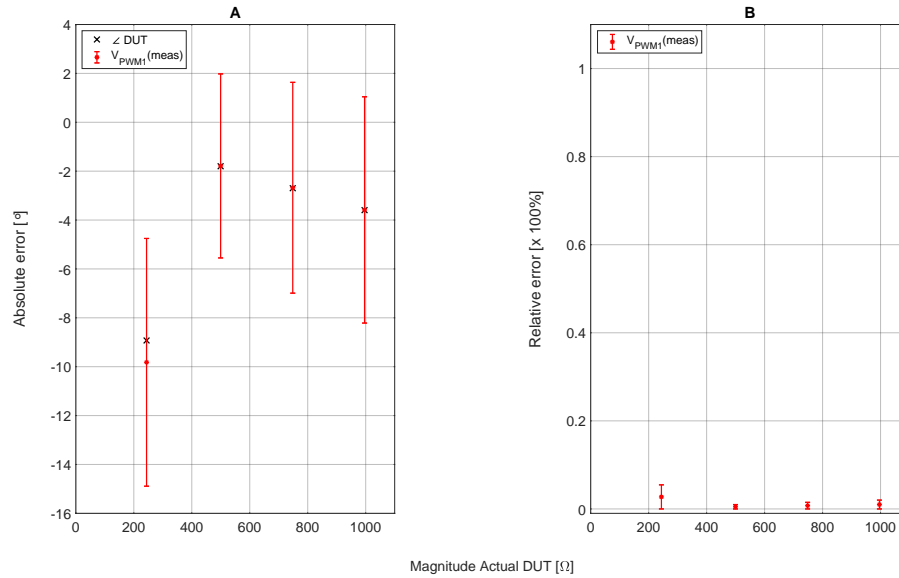


Figure 4.8: Phase measurements on a RC parallel combination as *DUT*: (A) The absolute phase error of $V_{P_{PWM1}}(meas)$ is evaluated with respect to $V_{P_{PWM,r}}(meas)$, and compared to the calculated phase of the *DUT*. (B) The relative phase error of $V_{P_{PWM1}}(meas)$ is evaluated with respect to $V_{P_{PWM,r}}(meas)$, and compared to the calculated phase of the *DUT*.

5

Discussion

5.1. Discussion

This thesis presents a new measurement instrumentation system for a wearable bioimpedance monitor in order to answer the main research question: *"How can the transthoracic bioimpedance be monitored remotely to provide continuous, accurate and reliable measurements in order to ensure self-management and comfort for patients with congestive heart failure?"*. Existing literature has shown conventional approaches to measure bioimpedance. In particular, analog-to-time based measurement approaches showed to be a feasible solution due to the simplicity and robustness. Research has presented that analog-to-time conversion methods can extract the magnitude and phase of a measured bioimpedance by employing only three comparators. Two comparators are required for one measurement channel and one comparator is employed to create a reference in order to acquire the phase information. Said approach reduces the amount of components needed compared to an analog-to-digital based approach, while ensuring similar stability against noise. However, the three comparator analog-to-time based suffers from the loss of information regarding the complete measured bioimpedance signal. Said approach solely provide the magnitude and phase at the output. Alternatively, an analog-to-time PWM-based approach modulates the entire measured bioimpedance signal into a PWM signal. Furthermore, PWM-based measurement approaches only requires one comparator per measurement channel. Therefore, it was hypothesized that the use of analog-to-time conversion employing PWM could lead to continuous, accurate and reliable measurements of the transthoracic bioimpedance.

5.1.1. Proposed PWM-based Measurement System

The proposed measurement instrumentation design employs a PWM-based analog-to-time conversion approach. Validation of said design was performed by means of simulations in LTspice[®] and measurement on the PCB prototype. Despite the correct efficacy of the designed system, the results show some limitations.

First of all, the *DUT* had a fixed upper limit of approximately 1 k Ω due to the fixed gain of the instrumentation amplifier. In practice, the gain is nonadjustable and, therefore upper limit of the *DUT* will always depend on the gain of the instrumentation amplifier. Second, the accuracy of the system clearly demonstrated limitation at low values of the *DUT*. At these condition, the resolution of the PWM output is low as well which causes the errors when measuring the magnitude and phase. In addition, the SNR of the instrumentation amplifier is decreased. Therefore, the noise the has more significance in the measured signal and causes the errors at low *DUT* values. Last, the gain and offset errors appear to be rather constant at high values of the *DUT*. Therefore, calibration can improve the accuracy of the system.

Improvements to the designed system would involve the choice of the instrumentation amplifiers. The instrumentation amplifier *AD8227* of *Texas Instruments* has an bipolar input stage. Therefore, an input bias current is required for the efficacy of the INA. For instance, an INA that employs a CMOS input stage would not require an input bias current. Also, to measure low magnitude *DUT* values the noise at the input of the INA is dominant. Therefore, the considering this in the design of the measurement channel can improve the accuracy.

5.1.2. System Level Architecture

The designed system followed the approach of a system level architecture to provide raw data without preprocessing at the output. Consequently, the time-to-digital conversion and the processing is moved to the receiver side. As presented in Section 2.2, said approach requires the transmission of a big amount of data compared to the method shown in [44]. However, the designed system provides a system level architecture which can be used in a modular approach depending on the application. Namely, in [53] in addition to bioimpedance measurements, ECG is measured simultaneously. Providing only the magnitude and phase information at the output of the system would eliminate the possibility to measure the ECG signal. Moreover, if no additional information is needed except for the magnitude and phase of the measured bioimpedance signal, preprocessing can be implemented with the use of simple additional logic components [47]. Lastly, in [46] a PWM-based measurement system is followed by a transmitter based on FSK. Instead, the designed system allow for other types of transmission techniques depending on the application, such as UWB [49].

5.2. Conclusion and Contributions

A transthoracic bioimpedance monitor requires a measurement instrumentation design which provides continuous, accurate and reliable measurements. It is important that the magnitude and phase can be extracted from the measured signal in order to determine the measured bioimpedance. The approaches taken in conventional implement power-hungry components such as an ADC or suffer from information loss.

This thesis proposed a PWM-based ATC method in order to convert the measured signal to time rather then directly to the digital domain. Therefore, the additional components are moved outside of the system to the receiver side, such as the TDC and the processing unit. Consequently, reducing the area and power consumption of the system. In addition to the measured data that is converted to a PWM signal, a reference PWM signal is employed as well. Therefore, the phase shift caused by the bioimpedance can be derived. Simulations and a PCB prototype implementation are used to validate the proposed design. First of all, the efficacy of the implemented system was validated. It was shown that the measured analog signal and the reference were converted correctly to a PWM signal. In addition, initial sources of error could be characterized, such as the delay caused by the instrumentation amplifiers. Subsequently, the validation was performed by employing a *DUT* that varied between being resistive, capacitive, and a resistor and capacitor in parallel. The magnitude and phase were derived from the PWM output signals and the errors between the expected values were assessed. The results showed an increase in the error for low values of the *DUT*. This can be explained by noise that became more apparent under those conditions. Second, a sensitivity validation of the system was performed. The sampling frequency was increased for a fixed resistive *DUT*. The accuracy is directly proportional to the sampling frequency of the triangular wave..

In conclusion, the proposed design is able to accurately measure resistive and capacitive compositions of the *DUT*. Therefore, this work contributes to a wearable transthoracic bioimpedance monitor for continuous, accurate and reliable measurements.

5.3. Recommendations for Future Work

- **Excitation source**

In this work, an external voltage source $V_{ex,in}$ provide an AC voltage to the VCCS in order to generate the excitation current. This work didn't include design of the excitation source as part of the system. In the future, it would be required for the complete excitation source to be designed within the system in order to realize a wearable bioimpedance monitor. Therefore, future work should research design approaches, such as an analog implementation, or a digital implementation like a current digital-to-analog (I-DAC) implementation. Furthermore, this work has focused on single-frequency bioimpedance measurements. In order to perform a more complete bioimpedance measurement, future work should consider bioimpedance spectroscopy.

- **Electrodes**

The electrodes were not considered in the presented work. Therefore, future work should research what type of electrodes could be implemented along with the proposed system. Other research has shown gel-based adhesive electrode and textile-integrated electrodes. Furthermore,

the placement on the electrodes should also be investigated in the future since it determines the efficacy of the measurements. Last, this work solely included bipolar and tetrapolar electrode configuration. In future designs, multi-polar electrode configuration could be employed, such as in electrical impedance tomography.

- **Static and dynamic bioimpedance**

This work validated the proposed system using a variable *DUT*. The goal of said approach was to test if the system was able to measure a resistive, a capacitive or a RC-combination as *DUT*. As explained in [Section 2.3.2](#), the thoracic bioimpedance consists of a high-magnitude static bioimpedance and a small-magnitude dynamic bioimpedance. Future work should research the ability of the system to detect a small varying signal on top of a large static signal.

- **Receiver side**

The transmission of the PWM signals to the receiver side was not part of this thesis. In the future, transmitting the PWM signals should be research, similar as presented in [\[46\]](#), in order to investigate the effect on the accuracy of the received PWM signals. Furthermore, the implementation of a time-to-digital converter (TDC) should also be considered in order to process the data in the digital domain at the receiver side.

- **PCB improvements and circuit integration**

The PCB prototype developed in this work had the goal of validating the proposed design. Future prototypes could reduce the size of the PCB using smaller components, optimize the positioning of the components and utilize both top and bottom of the PCB. These improvements might help with the initial wearable prototype. However, the ultimate goal would be to for the system to be integrated in a integrated circuit (IC). On the IC, the proposed system should be combined with the other blocks of a wearable bioimpedance monitor presented in [Fig. 3.1](#). Additionally, such a IC should be integrated along with the electrodes in the complete wearable device.

Bibliography

- [1] A. D. DeVore, J. Wosik, and A. F. Hernandez, "The Future of Wearables in Heart Failure Patients," *JACC: Heart Failure*, vol. 7, no. 11, pp. 922–932, 2019. [Online]. Available: <https://doi.org/10.1016/j.jchf.2019.08.008>
- [2] T. K. Bera, "Bioelectrical Impedance Methods for Noninvasive Health Monitoring: A Review," *Journal of Medical Engineering*, vol. 2014, pp. 1–28, 6 2014. [Online]. Available: <https://www.hindawi.com/journals/jme/2014/381251/>
- [3] T. Schlebusch, L. Röthlingshöfer, S. Kim, M. Köny, and S. Leonhardt, "On the Road to a Textile Integrated Bioimpedance Early Warning System for Lung Edema," in *2010 International Conference on Body Sensor Networks*. IEEE, 6 2010, pp. 302–307. [Online]. Available: <http://ieeexplore.ieee.org/document/5504772/>
- [4] P. Shyamkumar, P. Rai, S. Oh, M. Ramasamy, R. E. Harbaugh, and V. Varadan, "Wearable wireless cardiovascular monitoring using textile-based nanosensor and nanomaterial systems," *Electronics (Switzerland)*, vol. 3, no. 3, pp. 504–520, 2014.
- [5] W. M. F. Smith, "Epidemiology of congestive heart failure," *The American Journal of Cardiology*, vol. 55, no. 2, p. A3, 1985.
- [6] A. Faragli, D. Abawi, C. Quinn, M. Cvetkovic, T. Schlabs, E. Tahirovic, H.-D. Düngen, B. Pieske, S. Kelle, F. Edelmann, and A. Alogna, "The role of non-invasive devices for the telemonitoring of heart failure patients," *Heart Failure Reviews*, vol. 26, no. 5, pp. 1063–1080, 9 2021. [Online]. Available: <https://link.springer.com/10.1007/s10741-020-09963-7>
- [7] H. M. Krumholz, E. M. Parent, N. Tu, V. Vaccarino, Y. Wang, M. J. Radford, and J. Hennen, "Readmission after hospitalization for congestive heart failure among medicare beneficiaries," *Archives of internal medicine*, vol. 157, no. 1, pp. 99–104, 1997.
- [8] C.-P. Lau, D. C. Siu, and H.-F. Tse, "Optimizing heart failure therapy with implantable sensors," *Journal of Arrhythmia*, vol. 28, no. 1, pp. 4–18, 2 2012. [Online]. Available: <http://dx.doi.org/10.1016/j.joa.2012.02.003><http://doi.wiley.com/10.1016/j.joa.2012.02.003>
- [9] C.-M. Yu, L. Wang, E. Chau, R. H.-W. Chan, S.-L. Kong, M.-O. Tang, J. Christensen, R. W. Stadler, and C.-P. Lau, "Intrathoracic Impedance Monitoring in Patients With Heart Failure," *Circulation*, vol. 112, no. 6, pp. 841–848, 8 2005. [Online]. Available: <https://www.ahajournals.org/doi/10.1161/CIRCULATIONAHA.104.492207>
- [10] M. Gheorghide, F. Follath, P. Ponikowski, J. H. Barsuk, J. E. Blair, J. G. Cleland, K. Dickstein, M. H. Drazner, G. C. Fonarow, T. Jaarsma, G. Jondeau, J. L. Sendon, A. Mebazaa, M. Metra, M. Nieminen, P. S. Pang, P. Seferovic, L. W. Stevenson, D. J. Van Veldhuisen, F. Zannad, S. D. Anker, A. Rhodes, J. J. McMurray, and G. Filippatos, "Assessing and grading congestion in acute heart failure: A scientific statement from the acute heart failure committee of the heart failure association of the European society of cardiology and endorsed by the European society of intensive care medicine," *European Journal of Heart Failure*, vol. 12, no. 5, pp. 423–433, 2010.
- [11] G. Charach, P. Rabinovich, I. Grosskopf, and M. Weintraub, "Transthoracic monitoring of the impedance of the right lung in patients with cardiogenic pulmonary edema," *Critical Care Medicine*, vol. 29, no. 6, pp. 1137–1144, 2001.
- [12] R. J. Goldberg, "Long-term Survival After Heart Failure," *Archives of Internal Medicine*, vol. 167, no. 5, p. 490, 3 2007. [Online]. Available: <https://linkinghub.elsevier.com/retrieve/pii/S0735109708017907><http://archinte.jamanetwork.com/article.aspx?doi=10.1001/archinte.167.5.490>

- [13] C. M. O'Connor, W. G. Stough, D. S. Gallup, V. Hasselblad, and M. Gheorghiade, "Demographics, clinical characteristics, and outcomes of patients hospitalized for decompensated heart failure: Observations from the IMPACT-HF registry," *Journal of Cardiac Failure*, vol. 11, no. 3, pp. 200–205, 2005.
- [14] J. E. Blair, S. Khan, M. A. Konstam, K. Swedberg, F. Zannad, J. C. Burnett, L. Grinfeld, A. P. Maggioni, J. E. Udelson, C. A. Zimmer, J. Ouyang, C. F. Chen, and M. Gheorghiade, "Weight changes after hospitalization for worsening heart failure and subsequent re-hospitalization and mortality in the EVEREST trial," *European Heart Journal*, vol. 30, no. 13, pp. 1666–1673, 2009.
- [15] S. Song, P. Vis, C. van Liempd, C. van Hoof, N. van Helleputte, M. Konijnenburg, R. van Wegberg, J. Xu, H. Ha, W. Sijbers, S. Stanzione, D. Biswas, and A. Breeschoten, "A 769 μ W Battery-Powered Single-Chip SoC With BLE for Multi-Modal Vital Sign Monitoring Health Patches," *IEEE Transactions on Biomedical Circuits and Systems*, vol. 13, no. 6, pp. 1506–1517, 12 2019. [Online]. Available: <https://ieeexplore.ieee.org/document/8854984/>
- [16] P. Kassanos, L. Constantinou, I. F. Triantis, and A. Demosthenous, "An integrated analog readout for multi-frequency bioimpedance measurements," *IEEE Sensors Journal*, vol. 14, no. 8, pp. 2792–2800, 2014.
- [17] W. R. Lionheart, J. Kaipio, and C. N. McLeod, "Generalized optimal current patterns and electrical safety in EIT," *Physiological Measurement*, vol. 22, no. 1, pp. 85–90, 2001.
- [18] U. KYLE, "Bioelectrical impedance analysis?part I: review of principles and methods," *Clinical Nutrition*, vol. 23, no. 5, pp. 1226–1243, 10 2004. [Online]. Available: <https://linkinghub.elsevier.com/retrieve/pii/S0261561404000937>
- [19] F. Zhang, B. Sanchez, S. B. Rutkove, Y. Yang, H. Zhong, J. Li, and Z. Teng, "Numerical estimation of fricke-morse impedance model parameters using single-frequency sinusoidal excitation," *Physiological Measurement*, vol. 40, no. 9, 2019.
- [20] A. T. Azar, *Modeling and Control of Dialysis Systems*, ser. Studies in Computational Intelligence, A. T. Azar, Ed. Berlin, Heidelberg: Springer Berlin Heidelberg, 2013, vol. 405. [Online]. Available: <http://link.springer.com/10.1007/978-3-642-27558-6>
- [21] D. Naranjo-Hernández, J. Reina-Tosina, and M. Min, "Fundamentals, Recent Advances, and Future Challenges in Bioimpedance Devices for Healthcare Applications," *Journal of Sensors*, vol. 2019, pp. 1–42, 7 2019. [Online]. Available: <https://www.hindawi.com/journals/js/2019/9210258/>
- [22] S. Kapoulea, C. Psychalinos, and A. S. Elwakil, "Simple Implementations of the Cole-Cole Models," *2nd Novel Intelligent and Leading Emerging Sciences Conference, NILES 2020*, pp. 99–102, 2020.
- [23] S. Grimnes and O. G. Martinsen, *Bioimpedance and bioelectricity basics*. Academic press, 2011.
- [24] B. Sanchez, A. S. Bandarenka, G. Vandersteen, J. Schoukens, and R. Bragos, "Novel approach of processing electrical bioimpedance data using differential impedance analysis," *Medical Engineering and Physics*, vol. 35, no. 9, pp. 1349–1357, 2013. [Online]. Available: <http://dx.doi.org/10.1016/j.medengphy.2013.03.006>
- [25] L. Wang, "Fundamentals of Intrathoracic Impedance Monitoring in Heart Failure," *The American Journal of Cardiology*, vol. 99, no. 10, pp. S3–S10, 5 2007. [Online]. Available: <https://linkinghub.elsevier.com/retrieve/pii/S0002914907002822>
- [26] W. W. Tang and W. Tong, "Measuring impedance in congestive heart failure: Current options and clinical applications," *American Heart Journal*, vol. 157, no. 3, pp. 402–411, 3 2009. [Online]. Available: <http://dx.doi.org/10.1016/j.ahj.2008.10.016https://linkinghub.elsevier.com/retrieve/pii/S000287030800906X>

- [27] S. Dovancescu, S. Saporito, I. H. F. Herold, H. H. M. Korsten, R. M. Aarts, and M. Mischi, "Monitoring thoracic fluid content using bioelectrical impedance spectroscopy and Cole modeling," *Journal of Electrical Bioimpedance*, vol. 8, no. 1, pp. 107–115, 8 2019. [Online]. Available: <https://content.sciendo.com/view/journals/joeb/8/1/article-p107.xml>
- [28] S. Dovancescu, J. S. Saczynski, C. E. Darling, J. Riistama, F. Sert Kuniyoshi, T. Meyer, R. Goldberg, and D. D. McManus, "Detecting Heart Failure Decompensation by Measuring Transthoracic Bioimpedance in the Outpatient Setting: Rationale and Design of the SENTINEL-HF Study," *JMIR Research Protocols*, vol. 4, no. 4, p. e121, 2015.
- [29] L. Beckmann, D. Van Riesen, and S. Leonhardt, "Optimal electrode placement and frequency range selection for the detection of lung water using Bioimpedance Spectroscopy," *Annual International Conference of the IEEE Engineering in Medicine and Biology - Proceedings*, pp. 2685–2688, 2007.
- [30] B. Taji, S. Shirmohammadi, V. Groza, and I. Batkin, "Impact of skin-electrode interface on electrocardiogram measurements using conductive textile electrodes," *IEEE Transactions on Instrumentation and Measurement*, vol. 63, no. 6, pp. 1412–1422, 2014.
- [31] H. Posada-Quintero, N. Reljin, C. Eaton-Robb, Y. Noh, J. Riistama, and K. Chon, "Analysis of Consistency of Transthoracic Bioimpedance Measurements Acquired with Dry Carbon Black PDMS Electrodes, Adhesive Electrodes, and Wet Textile Electrodes," *Sensors*, vol. 18, no. 6, p. 1719, 5 2018. [Online]. Available: <http://www.mdpi.com/1424-8220/18/6/1719>
- [32] C. E. Darling, S. Dovancescu, J. S. Saczynski, J. Riistama, F. Sert Kuniyoshi, J. Rock, T. E. Meyer, and D. D. McManus, "Bioimpedance-Based Heart Failure Deterioration Prediction Using a Prototype Fluid Accumulation Vest-Mobile Phone Dyad: An Observational Study," *JMIR Cardio*, vol. 1, no. 1, p. e1, 3 2017. [Online]. Available: <http://cardio.jmir.org/2017/1/e1/>
- [33] G. Huertas, A. Maldonado, A. Yufera, A. Rueda, and J. L. Huertas, "A Circuit for Cell-Culture Assays," *IEEE Transactions on Circuits and Systems II: Express Briefs*, vol. PP, no. 99, p. 1, 2014. [Online]. Available: <http://ieeexplore.ieee.org/lpdocs/epic03/wrapper.htm?arnumber=6998822>
- [34] C. Margo, J. Katrib, M. Nadi, and A. Rouane, "A four-electrode low frequency impedance spectroscopy measurement system using the AD5933 measurement chip," *Physiological Measurement*, vol. 34, no. 4, pp. 391–405, 2013.
- [35] T. K. Bera, "Applications of Electrical Impedance Tomography (EIT): A Short Review," *IOP Conference Series: Materials Science and Engineering*, vol. 331, no. 1, p. 012004, 3 2018. [Online]. Available: <https://iopscience.iop.org/article/10.1088/1757-899X/331/1/012004>
- [36] L. M. Roa, D. Naranjo, J. Reina-Tosina, A. Lara, J. A. Milán, M. A. Estudillo, and J. S. Oliva, *Applications of Bioimpedance to End Stage Renal Disease (ESRD)*. Berlin, Heidelberg: Springer Berlin Heidelberg, 2013, pp. 689–769. [Online]. Available: https://doi.org/10.1007/978-3-642-27458-9_14
- [37] Y. Yang, J. Wang, G. Yu, F. Niu, and P. He, "Design and preliminary evaluation of a portable device for the measurement of bioimpedance spectroscopy," *Physiological Measurement*, vol. 27, no. 12, 2006.
- [38] J. He, M. Wang, X. Li, G. Li, and L. Lin, "Pulse wave detection method based on the bio-impedance of the wrist," *Review of Scientific Instruments*, vol. 87, no. 5, 2016. [Online]. Available: <http://dx.doi.org/10.1063/1.4947514>
- [39] R. Casanella, O. Casas, and R. Pallàs-Areny, "Differential synchronous demodulator for modulating sensors and impedance measurements," *Measurement Science and Technology*, vol. 16, no. 8, pp. 1637–1643, 2005.
- [40] N. Li, H. Xu, Z. Zhou, Z. Sun, X. Xu, and W. Wang, "Wide bandwidth cell impedance spectroscopy based on digital auto balancing bridge method," *2011 IEEE Biomedical Circuits and Systems Conference, BioCAS 2011*, pp. 53–56, 2011.

- [41] Y. Liu, X. Qiao, G. Li, and L. Lin, "An improved device for bioimpedance deviation measurements based on 4-electrode half bridge," *Review of Scientific Instruments*, vol. 87, no. 10, p. 105107, 10 2016. [Online]. Available: <http://dx.doi.org/10.1063/1.4963658http://aip.scitation.org/doi/10.1063/1.4963658>
- [42] J. Riistama, J. Muehlsteff, H. Reiter, F. Sartor, and A. Sipilä, "Minimally obtrusive measurement devices for monitoring of cardiovascular parameters - An overview," *2014 8th Conference of the European Study Group on Cardiovascular Oscillations, ESGCO 2014*, no. Esgco, pp. 137–138, 2014.
- [43] H. Reiter, J. Muehlsteff, and A. Sipilä, "Medical application and clinical validation for reliable and trustworthy physiological monitoring using functional textiles: Experience from the HeartCycle and MyHeart project," *Proceedings of the Annual International Conference of the IEEE Engineering in Medicine and Biology Society, EMBS*, pp. 3270–3273, 2011.
- [44] Y. Wu, D. Jiang, M. Habibollahi, N. Almarri, and A. Demosthenous, "Time Stamp – A Novel Time-to-Digital Demodulation Method for Bioimpedance Implant Applications," *IEEE Transactions on Biomedical Circuits and Systems*, vol. 14, no. 5, pp. 997–1007, 10 2020. [Online]. Available: <https://ieeexplore.ieee.org/document/9149688/>
- [45] T. Sun, D. Holmes, S. Gawad, N. G. Green, and H. Morgan, "High speed multi-frequency impedance analysis of single particles in a microfluidic cytometer using maximum length sequences," *Lab on a Chip*, vol. 7, no. 8, p. 1034, 2007. [Online]. Available: <http://xlink.rsc.org/?DOI=b703546b>
- [46] M. Yin and M. Ghovanloo, "Using Pulse Width Modulation for Wireless Transmission of Neural Signals in Multichannel Neural Recording Systems," *IEEE Transactions on Neural Systems and Rehabilitation Engineering*, vol. 17, no. 4, pp. 354–363, 8 2009. [Online]. Available: <https://ieeexplore.ieee.org/document/5061588/>
- [47] S. J. Kweon, S. Shin, J. H. Park, J. H. Suh, and H. J. Yoo, "A CMOS low-power polar demodulator for electrical bioimpedance spectroscopy using adaptive self-sampling schemes," *Proceedings - 2016 IEEE Biomedical Circuits and Systems Conference, BioCAS 2016*, pp. 284–287, 2016.
- [48] J. Luprano, P. de Carvalho, B. Eilebrecht, J. Kortelainen, J. Muehlsteff, A. Sipilä, J. Sola, D. Teichmann, and M. Ulbrich, "HeartCycle: Advanced sensors for telehealth applications," in *2013 35th Annual International Conference of the IEEE Engineering in Medicine and Biology Society (EMBC)*. IEEE, 7 2013, pp. 6984–6987. [Online]. Available: <http://ieeexplore.ieee.org/document/6611165/>
- [49] D. Bao, Z. Zou, M. Baghaei Nejad, Y. Qin, and L.-R. Zheng, "A Wirelessly Powered UWB RFID Sensor Tag With Time-Domain Analog-to-Information Interface," *IEEE Journal of Solid-State Circuits*, vol. 53, no. 8, pp. 2227–2239, 8 2018. [Online]. Available: <https://ieeexplore.ieee.org/document/8355728/>
- [50] F. Chen, A. P. Chandrakasan, and V. M. Stojanovic, "Design and Analysis of a Hardware-Efficient Compressed Sensing Architecture for Data Compression in Wireless Sensors," *IEEE Journal of Solid-State Circuits*, vol. 47, no. 3, pp. 744–756, 3 2012. [Online]. Available: <http://ieeexplore.ieee.org/document/6155205/>
- [51] Jong Cheol Baeg, Hun Wi, Tong In Oh, A. McEwan, and Eung Je Woo, "An Amplitude-to-Time Conversion Technique Suitable for Multichannel Data Acquisition and Bioimpedance Imaging," *IEEE Transactions on Biomedical Circuits and Systems*, vol. 7, no. 3, pp. 349–354, 6 2013. [Online]. Available: <http://ieeexplore.ieee.org/document/6316094/>
- [52] M. Yin, R. Field, and M. Ghovanloo, "A 15-channel wireless neural recording system based on time division multiplexing of pulse width modulated signals," *Proceedings of 2006 International Conference on Microtechnologies in Medicine and Biology*, pp. 297–300, 2006.

- [53] J. Xu, P. Harpe, and C. Van Hoof, "An Energy-Efficient and Reconfigurable Sensor IC for Bio-Impedance Spectroscopy and ECG Recording," *IEEE Journal on Emerging and Selected Topics in Circuits and Systems*, vol. 8, no. 3, pp. 616–626, 9 2018. [Online]. Available: <https://ieeexplore.ieee.org/document/8355772/>
- [54] S. Weyer, M. D. Zink, T. Wartzek, L. Leicht, K. Mischke, T. Vollmer, and S. Leonhardt, "Bioelectrical impedance spectroscopy as a fluid management system in heart failure," *Physiological Measurement*, vol. 35, no. 6, pp. 917–930, 2014.
- [55] L. Beckmann, C. Neuhaus, G. Medrano, N. Jungbecker, M. Walter, T. Gries, and S. Leonhardt, "Characterization of textile electrodes and conductors using standardized measurement setups," *Physiological Measurement*, vol. 31, no. 2, pp. 233–247, 2010.
- [56] M. Ulbrich, J. Mühlsteff, D. Teichmann, S. Leonhardt, and M. Walter, "A thorax simulator for complex dynamic bioimpedance measurements with textile electrodes," *IEEE Transactions on Biomedical Circuits and Systems*, vol. 9, no. 3, pp. 412–420, 2015.
- [57] J. Xu, P. Harpe, J. Pettine, C. Van Hoof, and R. F. Yazicioglu, "A low power configurable bio-impedance spectroscopy (BIS) ASIC with simultaneous ECG and respiration recording functionality," in *ESSCIRC Conference 2015 - 41st European Solid-State Circuits Conference (ESSCIRC)*, vol. 2015-Octob. IEEE, 9 2015, pp. 396–399. [Online]. Available: <http://ieeexplore.ieee.org/document/7313911/>
- [58] S. Hersek, H. Toreyin, and O. T. Inan, "A Robust System for Longitudinal Knee Joint Edema and Blood Flow Assessment Based on Vector Bioimpedance Measurements," *IEEE Transactions on Biomedical Circuits and Systems*, vol. 10, no. 3, pp. 545–555, 6 2016. [Online]. Available: <https://ieeexplore.ieee.org/document/7365493/>
- [59] M. Zamani, Y. Rezaeiyan, O. Shoaee, and W. A. Serdijn, "A 1.55 μ W Bio-Impedance Measurement System for Implantable Cardiac Pacemakers in 0.18 μ m CMOS," *IEEE Transactions on Biomedical Circuits and Systems*, vol. 12, no. 1, pp. 211–221, 2 2018. [Online]. Available: <https://ieeexplore.ieee.org/document/8248760/>
- [60] J. Daniels, W. Dehaene, M. S. Steyaert, and A. Wiesbauer, "A/D conversion using asynchronous delta-sigma modulation and time-to-digital conversion," *IEEE Transactions on Circuits and Systems I: Regular Papers*, vol. 57, no. 9, pp. 2404–2412, 2010.
- [61] J. Caldwell, "Analog Pulse Width Modulation," *Analog Pulse Width Modulation*, vol. 3, no. June, pp. 1–21, 2013. [Online]. Available: <http://www.ti.com>
- [62] J. Huang, K. Padmanabhan, and O. M. Collins, "The Sampling Theorem With Constant Amplitude Variable Width Pulses," *IEEE Transactions on Circuits and Systems I: Regular Papers*, vol. 58, no. 6, pp. 1178–1190, 6 2011. [Online]. Available: <http://ieeexplore.ieee.org/document/5699377/>
- [63] M. Yin and M. Ghovanloo, "A wideband PWM-FSK receiver for wireless implantable neural recording applications," *Proceedings - IEEE International Symposium on Circuits and Systems*, pp. 1556–1559, 2008.
- [64] S.-J. Kweon, J.-H. Park, S. Shin, S.-S. Yoo, and H.-J. Yoo, "A reconfigurable time-to-digital converter based on time stretcher and chain-delay-line for electrical bioimpedance spectroscopy," in *2017 IEEE 60th International Midwest Symposium on Circuits and Systems (MWSCAS)*, vol. 6. IEEE, 8 2017, pp. 1037–1040. [Online]. Available: <http://ieeexplore.ieee.org/document/8053104/>
- [65] C. Verhoeven, "First order oscillators," Ph.D. dissertation, Delft University of Technology, 1990. [Online]. Available: <https://repository.tudelft.nl/islandora/object/uuid%3Aadf76c81-fb5d-45d7-b8ce-4428bd10c6b0>